



TECHNICKÁ UNIVERZITA V LIBERCI  
Fakulta strojní



# Experimental Investigation of the Continual Jet

## Diplomová práce

*Studijní program:* N2301 – Mechanical Engineering  
*Studijní obor:* 2302T010 – Machines and Equipment Design  
*Autor práce:* **Sudarshan Shamsundar Boob**  
*Vedoucí práce:* Ing. Petra Dančová, Ph.D.





# Experimental Investigation of the Continual Jet

## Master thesis

*Study programme:* N2301 – Mechanical Engineering  
*Study branch:* 2302T010 – Machines and Equipment Design  
*Author:* **Sudarshan Shamsundar Boob**  
*Supervisor:* Ing. Petra Dančová, Ph.D.





## Master Thesis Assignment Form

# Experimental Investigation of the Continual Jet

*Name and Surname:* **Sudarshan Shamsundar Boob**  
*Identification Number:* S17000499  
*Study Programme:* N2301 Mechanical Engineering  
*Specialisation:* Machines and Equipment Design  
*Assigning Department:* Department of Power Engineering Equipment  
*Academic Year:* **2018/2019**

### Rules for Elaboration:

1. Make the "state of art" of the problem.
2. Perform the velocity fields experiments with the 3D PIV and evaluate the pressure fields.
3. Analyze the data and do the comparison with the literature.



Scope of Report:

up to 50 pages

Thesis Form:

printed

Thesis Language:

English



**List of Specialised Literature:**

[1] WIENEKE, Bernhard. PIV Uncertainty Quantification and Beyond. *Unpublished* [online]. 2017 [vid. 2019-04-25]. Dostupné z: doi:10.13140/rg.2.2.26244.42886

[2] NEETESON, N. J., S. BHATTACHARYA, D. E. RIVAL, D. MICHAELIS, D. SCHANZ a A. SCHRÖDER. Pressure-field extraction from Lagrangian flow measurements: first experiences with 4D-PTV data. *Experiments in Fluids* [online]. 2016, 57(6) [vid. 2019-04-25]. ISSN 0723-4864, 1432-1114. Dostupné z: doi:10.1007/s00348-016-2170-4

Thesis Supervisor:

Ing. Petra Dančová, Ph.D.  
Department of Power Engineering Equipment

Date of Thesis Assignment:

1 November 2018

Date of Thesis Submission:

30 April 2020

prof. Dr. Ing. Petr Lenfeld  
Dean

Liberec 1 February 2019



  
doc. Ing. Václav Dvořák, Ph.D.  
Head of Department



## Declaration

I hereby certify I have been informed that my master thesis is fully governed by Act No. 121/2000 Coll., the Copyright Act, in particular Article 60 – School Work.

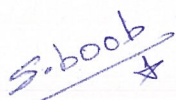
I acknowledge that the Technical University of Liberec (TUL) does not infringe my copyrights by using my master thesis for the TUL's internal purposes.

I am aware of my obligation to inform the TUL on having used or granted license to use the results of my master thesis; in such a case the TUL may require reimbursement of the costs incurred for creating the result up to their actual amount.

I have written my master thesis myself using the literature listed below and consulting it with my thesis supervisor and my tutor.

At the same time, I honestly declare that the texts of the printed version of my master thesis and of the electronic version uploaded into the IS STAG are identical.

3. 5. 2019

  
Sudarshan Shamsundar Boob

## **ACKNOWLEDGEMENT**

All praises belongs to Almighty God, the most merciful, the most beneficent and the most kind for giving me the opportunity, courage and enough energy to carry out and complete the entire thesis work.

I am grateful and deeply indebted to my guide Professor Dr. Petra Dančová. I have the great privilege and honour to express my whole hearted indebtedness to her for kindly placing at my disposal all the facilities available in the department for her guidance, supervision, inspiring encouragement and help in carrying out this thesis work.

Lastly, I would like to thank my family and friends for being helpful and supportive throughout my studies.

## ABSTRACT

This thesis work primarily focusses on the study of the structure and development of the free jet generated through the round air jet nozzle. It also involves the study of the velocity fields generated by round jet at the nozzle exit velocity 5.67 m/s and with corresponding Reynolds number of 3070. The investigation was carried out in 2D (stereo PIV) and 3D (Tomo PIV). The scope of the study was further extended to understand the characteristics of all three velocity components in the developing shear layer and deriving the pressure fields over the space using the available velocity field data. Pulsed laser sheets were aligned such that it illuminates the centreline plane of the jet. The set-up was calibrated to translate the resulting pixel displacements into X, Y, and Z velocity components. The measurement was done with varying the laser power and varying the laser pulse time i.e. delay time. For measurement of the Tomo PIV the volume optics were used also volume self-calibration were carried out. The tracer particles used in the experiment were generated from the vegetable oil and compressed air was used for providing the necessary acceleratory movement to the particles.

The result helped to study the different structures and development of the free jet along its centreline axis direction. The velocity range over entire field and pressure variations along the streamline axis are discussed. The maximum particle velocity was found to be 25 m/s in the jet core.

# TABLE OF CONTENTS

<b>1</b>	<b>INTRODUCTION .....</b>	<b>1</b>
1.1	STRUCTURE AND DEVELOPMENT OF A FREE JET .....	1
1.2	FACTORS INFLUENCING JET SPREAD .....	2
1.2.1	INLET VELOCITY PROFILE.....	3
1.2.2	NOZZLE GEOMETRY .....	3
1.2.3	JET REYNOLDS NUMBER.....	4
1.2.4	JET INSTABILITIES.....	4
1.2.5	COHERENT STRUCTURES.....	5
1.2.6	ASPECT RATIO .....	5
1.3	VORTICITY .....	6
1.3.1	VORTEX DETECTION .....	6
<b>2</b>	<b>INTRODUCTION TO PARTICLE IMAGE VELOCIMETRY (PIV) .....</b>	<b>8</b>
2.1	PHYSICAL AND TECHNICAL BACKGROUND .....	8
2.2	PRINCIPLE OF PARTICLE IMAGE VELOCIMETRY (PIV) .....	8
2.3	SOME GENERAL ASPECTS OF THE PIV METHOD .....	9
2.4	PIV COMPONENTS.....	12
2.4.1	TRACER PARTICLES.....	12
2.4.2	LIGHT SCATTERING BEHAVIOUR .....	13
2.4.3	GENERATION OF PARTICLE .....	15
2.4.4	OIL DROPLET SEEDING OF AIR FLOW .....	15
2.4.5	LIGHT SOURCES .....	16
2.5	PIV RECORDING TECHNIQUES.....	19
2.5.1	SINGLE FRAME/MULTI-EXPOSURE RECORDING.....	20
2.5.2	DOUBLE FRAME/MULTI-EXPOSURE RECORDING.....	21
2.6	IMAGE EVALUATION METHOD FOR PIV .....	22
2.7	STEREO PIV .....	25
2.7.1	RECONSTRUCTION GEOMETRY .....	26
2.7.2	STEREO VIEWING CALIBRATION .....	28
2.7.3	CAMERA CALIBRATION .....	29
2.7.4	DISPARITY CORRECTION .....	30
2.7.5	STEREOSCOPIC CONFIGURATION .....	31



2.8	TOMOGRAPHIC-PIV INTRODUCTION.....	35
2.8.1	INTRODUCTION TOMOGRAPHIC PARTICLE IMAGE VELOCIMETRY.....	35
2.8.2	WORKING PRINCIPLE OF TOMOGRAPHIC-PIV .....	35
2.8.3	TOMOGRAPHIC RECONSTRUCTION ALGORITHM .....	36
2.8.4	ALGEBRAIC METHODS .....	36
2.9	PIV ERROR CORRECTION.....	38
2.9.1	CORRELATION ERRORS.....	39
2.9.2	CORRELATION ERROR CORRECTION .....	40
2.10	PIV UNCERTAINTY QUANTIFICATION .....	40
2.11	PIV ERROR SOURCES .....	41
2.11.1	TIMING AND SYNCHRONIZATION ERRORS .....	42
2.11.2	STEREO-PIV ERRORS .....	42
2.12	MEASUREMENT OF PRESSURE DISTRIBUTION FROM PIV EXPERIMENTS .....	43
<b>3</b>	<b>EXPERIMENTAL SETUP AND MEASUREMENTS.....</b>	<b>46</b>
3.1	COMPONENTS AND THERE SPECIFICATIONS .....	46
3.2	MEASUREMENTS.....	49
3.2.1	STEREO PIV .....	50
3.2.2	TOMO-PIV .....	50
<b>4</b>	<b>RESULTS AND DISCUSSION .....</b>	<b>51</b>
4.1	STEREO PIV .....	51
4.2	TOMO-PIV .....	57
<b>5</b>	<b>CONCLUSION.....</b>	<b>64</b>
5.1	FUTURE WORK.....	64
	<b>REFERENCES.....</b>	<b>65</b>

# LIST OF FIGURES

<b>FIGURE 1</b>	STRUCTURE AND DEVELOPMENT OF THE FREE JET .....	2
<b>FIGURE 2</b>	SHEAR LAYER INSTABILITIES IN A JET .....	4
<b>FIGURE 3</b>	ASPECT RATIO OF A RECTANGULAR JET NOZZLE.....	5
<b>FIGURE 4</b>	BEHAVIOUR OF AUTONOMOUS ORDINARY DIFFERENTIAL EQUATIONS OF TWO DEGREES OF FREEDOM IN DIFFERENT REGIONS DEPENDENT ON TRACE AND DETERMINANT OF THE VELOCITY GRADIENT TENSOR GIVEN IN EQUATION. ....	6
<b>FIGURE 5</b>	GENERAL SET UP DEMONSTRATING PIV WORKING PRINCIPLE .....	9
<b>FIGURE 6</b>	THE THREE MODES OF PARTICLE IMAGE DENSITY: A) LOW (PTV), B) MEDIUM (PIV), AND C) HIGH IMAGE DENSITY (LSV). ....	11
<b>FIGURE 7</b>	TIME RESPONSE OF OIL PARTICLES WITH DIFFERENT DIAMETERS IN A DECELERATING AIR FLOW .....	13
<b>FIGURE 8</b>	LIGHT SCATTERING BY A $1\mu m$ OIL PARTICLE IN .....	14
<b>FIGURE 9</b>	LIGHT SCATTERING BY $10\mu m$ OIL PARTICLE IN .....	14
<b>FIGURE 10</b>	SEEDING PARTICLE GENERATOR .....	16
<b>FIGURE 11</b>	SKETCH OF LASKIN NOZZLE .....	16
<b>FIGURE 12</b>	SCHEMATIC DIAGRAM OF LASER .....	16
<b>FIGURE 13</b>	ELEMENTARY KINDS OF INTERACTIONS BETWEEN ATOMS AND ELECTROMAGNETIC RADIATION .....	17
<b>FIGURE 14</b>	EVOLUTION OF THE LIGHT SHEET PROFILE WITH INCREASING DISTANCE FROM THE LASER .....	19
<b>FIGURE 15</b>	SINGLE FRAME TECHNIQUES .....	20
<b>FIGURE 16</b>	ELIMINATION OF THE AMBIGUITY OF DIRECTION OF THE DISPLACEMENT VECTOR AS OBSERVED IN THE RECORDING PLANE .....	21
<b>FIGURE 17</b>	MULTIPLE FRAME TECHNIQUES (OPEN CIRCLES INDICATE THE PARTICLES POSITIONS IN THE PREVIOUS FRAMES.) .....	21
<b>FIGURE 18</b>	ANALYSIS OF SINGLE FRAME/DOUBLE EXPOSURE RECORDINGS THE FULLY DIGITAL AUTOCORRELATIONS METHOD .....	22
<b>FIGURE 19</b>	ANALYSIS OF DOUBLE FRAME/SINGLE EXPOSURE RECORDINGS: THE DIGITAL CROSS CORRELATION METHOD .....	23
<b>FIGURE 20</b>	ANALYSIS OF SINGLE FRAME/DOUBLE EXPOSURE CROSS CORRELATION METHOD ..	23
<b>FIGURE 21</b>	ANALYSIS OF SINGLE FRAME/DOUBLE EXPOSURE RECORDINGS: THE FULLY OPTICAL METHOD .....	24
<b>FIGURE 22</b>	BASIC STEREOSCOPIC IMAGING CONFIGURATIONS .....	26
<b>FIGURE 23</b>	STEREO VIEWING GEOMETRY IN THE XZ-PLANE .....	27
<b>FIGURE 24</b>	THE BACK-PROJECTION ALGORITHM HAS TO MAP THE RECORDED IMAGE ON THE LEFT TO THE RECONSTRUCTED IMAGE ON THE RIGHT . ....	29
<b>FIGURE 25</b>	PRECISION MACHINED TWIN LEVEL CALIBRATION TARGET WITH DOT PATTERN FOR STEREO PIV CALIBRATION. LEVELS ARE SEPARATED BY 2 MM; DOTS ARE EQUALLY SPACED ON A 10MM GRID. ....	30
<b>FIGURE 26</b>	MISALIGNMENT BETWEEN CALIBRATION TARGET AND LIGHT SHEET PLANE RESULTS IN A MISMATCH BETWEEN THE ACTUAL IMAGED AREAS .....	30

<b>FIGURE 27</b>	<b>SCHEMATIC OF STEREO CAMERA IN THE TRANSLATION CONFIGURATION .....</b>	<b>31</b>
<b>FIGURE 28</b>	<b>BASIC CONFIGURATION FOR STEREOSCOPIC PIV SYSTEMS: ANGULAR- DISPLACEMENT METHOD .....</b>	<b>33</b>
<b>FIGURE 29</b>	<b>NON-UNIFORMITY IN MAGNIFICATION ACROSS THE OBJECT PLANE IN THE SCHEIMPFLUG SYSTEM FOR NOMINAL MAGNIFICATIONS VARYING BETWEEN 0.2 AND 1.0 IN STEPS OF 0.2: A) <math>\theta = 15^\circ</math>, B) <math>\theta = 30^\circ</math>, C) <math>\theta = 45^\circ</math> .....</b>	<b>34</b>
<b>FIGURE 30</b>	<b>STEREOSCOPIC ARRANGEMENT WITH CAMERA ON EITHER SIDE OF THE LIGHT SHEET .....</b>	<b>34</b>
<b>FIGURE 31</b>	<b>PRINCIPLE OF TOMOGRAPHIC – PIV .....</b>	<b>35</b>
<b>FIGURE 32</b>	<b>REPRESENTATION OF THE IMAGING MODEL USED FOR TOMOGRAPHIC RECONSTRUCTION. IN THIS TOP-VIEW THE IMAGE PLANE IS SHOWN AS A LINE OF PIXEL ELEMENTS AND THE MEASUREMENT VOLUME IS A 2D ARRAY OF VOXELS. THE GREY LEVEL INDICATES THE VALUE OF THE WEIGHTING COEFFICIENT IN EACH OF THE VOXEL WITH RESPECT TO THE PIXEL L (<math>X_L</math>, <math>Y_L</math>) .....</b>	<b>37</b>
<b>FIGURE 33</b>	<b>ELIMINATION OF CORRELATION ANOMALIES BY MULTIPLYING THE CORRELATION TABLES FROM ADJACENT REGIONS. CORRELATION VALUES THAT DO NOT APPEAR IN BOTH TABLES ARE ELIMINATED ALLOWING TRACER PARTICLE DISPLACEMENT TO BE RESOLVED. ....</b>	<b>40</b>
<b>FIGURE 34</b>	<b>OVERVIEW OF PIV ERROR SOURCES .....</b>	<b>41</b>
<b>FIGURE 35</b>	<b>STEREO PIV SELF-CALIBRATION PROCEDURE CORRECTING MISALIGNMENT OF LASER SHEET .....</b>	<b>42</b>
<b>FIGURE 36</b>	<b>CONTROL-VOLUME APPROACH FOR DETERMINING INTEGRAL FORCES FROM TWO DIMENSIONAL FLOW .....</b>	<b>44</b>
<b>FIGURE 37</b>	<b>EXPERIMENTAL SETUP .....</b>	<b>46</b>
<b>FIGURE 38</b>	<b>ORIENTATION OF THE CAMERA .....</b>	<b>46</b>
<b>FIGURE 39</b>	<b>SCHEIMPFLUG ADAPTER .....</b>	<b>47</b>
<b>FIGURE 40</b>	<b>NOZZLE .....</b>	<b>47</b>
<b>FIGURE 41</b>	<b>PARTICLE GENERATOR .....</b>	<b>47</b>
<b>FIGURE 42</b>	<b>DUAL PULSED LASER.....</b>	<b>47</b>
<b>FIGURE 43</b>	<b>Q-SWITCH PRINCIPLE .....</b>	<b>48</b>
<b>FIGURE 44</b>	<b>FLASH LAMP TO Q-SWITCH PRINCIPLE .....</b>	<b>48</b>
<b>FIGURE 45</b>	<b>CALIBRATION PLATE .....</b>	<b>49</b>
<b>FIGURE 46</b>	<b>CALIBRATION PLATE IMAGE FROM THE SYSTEM AFTER CALIBRATION (STEREOPIV).....</b>	<b>49</b>
<b>FIGURE 47</b>	<b>STRUCTURAL DEVELOPMENT OF THE FREE JET ALONG THE AXIAL DIRECTION OF THE STREAM. ....</b>	<b>51</b>
<b>FIGURE 48</b>	<b>FLOW CHARACTERISTICS OF THE STEREO PIV MEASUREMENT WITH 30MS LASER PULSE TIME AND 3% LASER POWER .....</b>	<b>55</b>
<b>FIGURE 49</b>	<b>ISO-SURFACE GENERATED AT THE NOZZLE EXIT A) AXIAL VELOCITY COMPONENT B) VORTICITY .....</b>	<b>58</b>
<b>FIGURE 50</b>	<b>VECTOR SLICES OF THE VELOCITY FOR THE AXIAL COMPONENT OF THE VELOCITY (A) AT <math>Z=-5</math> (B) <math>Z=0</math> (C) <math>Z=5</math>.....</b>	<b>60</b>
<b>FIGURE 51</b>	<b>THE VORTICITY BEHAVIOUR AT A) <math>Z=-5</math> B) <math>Z=0</math> C) <math>Z=5</math> .....</b>	<b>61</b>
<b>FIGURE 52</b>	<b>TIME AVERAGED PRESSURE OVER THE FLOW FIELD .....</b>	<b>62</b>

## LIST OF TABLES

<b>TABLE 1</b> SEEDING MATERIALS FOR GAS FLOWS .....	14
<b>TABLE 2</b> SEEDING MATERIALS FOR LIQUID FLOWS .....	15
<b>TABLE 3</b> OTHER IMPORTANT PARAMETERS FOR MEASUREMENT.....	49
<b>TABLE 4</b> STEREO-PIV MEASUREMENT .....	50
<b>TABLE 5</b> TOMO-PIV MEASUREMENT .....	50

## LIST OF GRAPHS

<b>GRAPH 1</b> GRAPHICAL REPRESENTATION OF THE A) U-COMPONENT OF THE VELOCITY B) V- COMPONENT OF THE VELOCITY C) W- COMPONENT OF THE VELOCITY .....	57
<b>GRAPH 2</b> GRAPHICAL REPRESENTATION OF THE A) U-COMPONENT OF THE VELOCITY B) V- COMPONENT OF THE VELOCITY C) W- COMPONENT OF THE VELOCITY.....	63

# 1 INTRODUCTION

Recent times the research and study of the jets has been in the lime light. The reason for this the jets the characteristic can be used over a wide applications. In particularly the circular and the planar jets have found some significant industrial applications like drying processes in the industry, air curtains for the preventing the air infiltration losses in the ventilation and air conditioning. During these processes the parameters like jet spray rate and potential core decay play a strong role in determining the efficiency of the final mixing process. So it has been very necessary for us to learn the fluid flow characteristics of the jets.[1]

Free jet can be explained as pressure driven unrestricted flow. As we know the fluid boundary cannot sustain a pressure difference across the subsonic boundary of jet acts as free shear layer in this the static pressure is constant all over the layer. The boundary layer acts as the free shear layer at the end of the device exit. At the exit the ambient fluid is entrained in the jet flow this result in the increase of the mass flow rate as the flow proceeds further in the downstream. The centre line velocity goes on decreasing as the flow proceeds further in the downstream direction. This can be justified by the scientific term known as conservation of the momentum. [1]

## 1.1 STRUCTURE AND DEVELOPMENT OF A FREE JET

Free jet can be explained as the certain mass of fluid entering into the environment having the infinite amount of the ambient fluid. There has been a previous research done for knowing the flow structures in the free jet. The study has identified four basic zones which are completely defined on the basis of the centreline velocity decay.

### **Convergent Zone (Zone 1)**

This is the potential core of the jet. The centreline velocity of the jet here is equal to the nozzle exit velocity. This area is extended over  $4d$  to  $6d$  where  $d$  is the diameter of the jet nozzle.

### **Transition zone (Zone 2)**

This is the area where the centreline velocity of the jet starts to decay. The velocity in this



area can be empirically denoted by  $X^{-0.5}$ , where  $x$  is the axial distance. The extension of this area is over  $6d$  to  $20d$ .

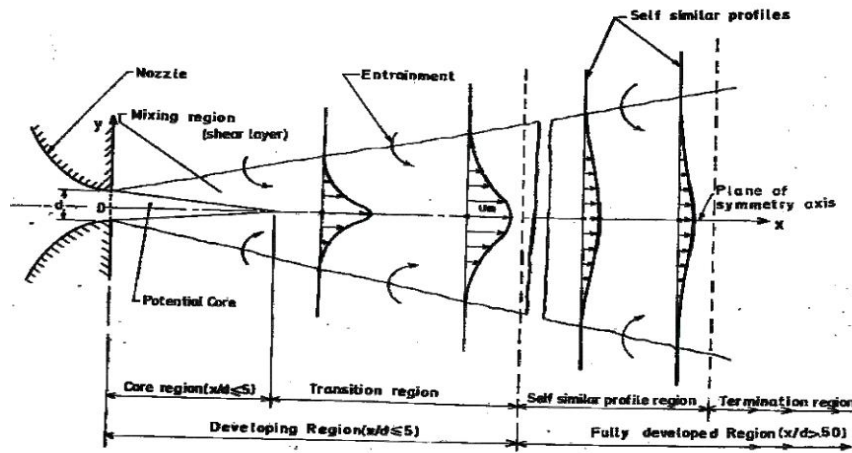


Figure 1 Structure and development of the free jet [2]

### Self-similar zone (Zone 3)

Over this region the transverse velocity profiles shows the similarity with the different values of the  $X$ . The empirical formula for the velocity decay can be given by  $X^{-1}$ .

### Termination Zone (Zone 4)

This zone shows the termination of the velocity termination pattern. Over this region there is great depletion of the centreline velocity.

Comparing all the 4 ones described above mainly first three zones has found application in the engineering field. The large velocity difference at the surface of discontinuity between jet fluid and ambient fluid is formed; this leads to lateral mixing of the fluid. As consequences of this jet fluid velocity is decreased whereas the ambient fluid velocity is increased. This entrainment of the ambient fluid with the jet fluid leads to increase in the width of the jet. [3]

## 1.2 FACTORS INFLUENCING JET SPREAD

There are many factors which influences the jet velocity profiles amongst them mainly Reynolds number, nozzle geometry, inlet velocity profile and fluid inlet temperature plays important role. These factors are discussed in brief below:



### 1.2.1 INLET VELOCITY PROFILE

The inlet properties of the fluid as the great influence on the jet profile. The jet inlet profile can be classified into four types: laminar, nominally laminar, highly disturbed and fully turbulent. If the inlet jet conditions are laminar and fully turbulent then typically second and third case is achieved. The shear layer at the jet inlet shows the mean velocity profile. These having the peak values can be seen near the jet boundaries are result of the shear layer instability. Generally the spectrum for the laminar shear flow has typically few peaks. The parameters needed to get the actual conditions of the nozzle exit.

$$\begin{aligned} \text{Displacement thickness} \quad \delta &= \int_{-\infty}^{\infty} \left(1 - \frac{U}{U_{\infty}}\right) dy & (1.1) \\ \theta &= \end{aligned}$$

$$\text{Momentum thickness} \quad \int_{-\infty}^{\infty} \frac{U}{U_{\infty}} \left(1 - \frac{U}{U_{\infty}}\right) dy \quad (1.2)$$

$$\text{Shape Factor} \quad H = \frac{\delta}{\theta} \quad (1.3)$$

The value of the shape factor is 2.5 for a laminar boundary condition at nozzle exit goes on decreasing to 1.4 fully turbulent flows. The other transitional boundary layers can be found in this range.[2]

### 1.2.2 NOZZLE GEOMETRY

The nozzle geometry has greater influence over the mean centreline velocity. As discussed above the empirical formula for it is different for the round and plane jet. The transitional characteristics of the jet are also dependent upon the nozzle cross-sectional shape. The rectangular jets with higher aspect ratios follows phenomenon of the axis switching. This phenomenon can be described as switch between the major and minor axes with the axial distance. The reason behind this phenomenon is the there is two different spread rate as across two lateral directions. This phenomenon is absent in case of the round nozzle. Also the nozzle geometry has impact on the inlet velocity profile. For example, shard edged orifice geometry may cause saddle-backed initial velocity profile where in case of the smooth contraction nozzle top hat profile is obtained. [2]



### 1.2.3 JET REYNOLDS NUMBER

For plane jet Reynolds number can be given by

$$Re = \frac{U_o d}{\nu} \quad (1.4)$$

Where  $d$  is the height of the nozzle, bulk mean velocity  $U_o$  and kinematic viscosity  $\nu$ .

In plane nozzle jet inlet velocity variation will be hat profile and bulk mean velocity is near to the nozzle exit.

It has been evident from the previous studies that if the Reynolds number at the nozzle exit is very high typically in several thousand radial spread of the mean velocity field and the decay of the mean centreline velocity towards the downstream direction are independent of Reynolds number. For the jet with very low Reynolds no (less than 30) the jet is called dissipated laminar jet. If the Reynolds no of the jet is around 500 the jet has some length over which the jet behaves as laminar after that it starts to behave as turbulent flow. For the Reynolds no above 2000 the jet becomes turbulent at very close to the nozzle exit area.

For the values of the Reynolds no between 13000 to 22000 for round jets the mean flow in the near-field (up to 10 nozzle exit diameters) has been studied and the study has shown entrainment or the each nozzle was found to be independent of the Reynolds number. The similar studies also has proved that the entrainment coefficient decreases with the increase of the Reynolds no up to 10,000. Beyond this value of the Reynolds no the coefficient becomes constant. Similar results were found for the slot jet.

The investigation of the turbulent structure in the developing region tells us that the maximum turbulent intensity occur for the station of  $x/d=6$ , which is approximately very close to the end of potential core.[4]

### 1.2.4 JET INSTABILITIES

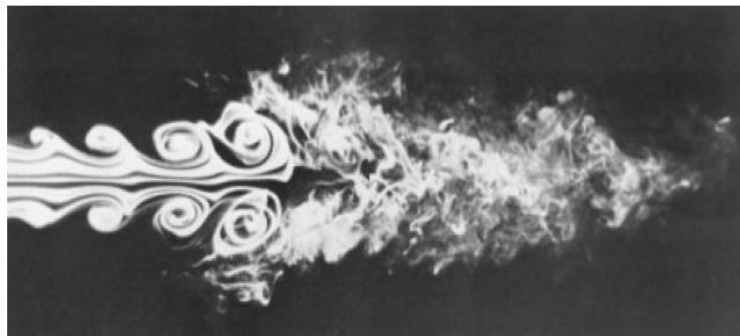


*Figure 2 Shear layer instabilities in a jet [2]*



The fluid jet after its discharge in the normal environment develops flow oscillations in the shear layer these flow oscillations are greatly influenced by the initial velocity profile. These oscillations are the main reason behind the vortices and the size and strength of them goes on increasing with its axial distance. These newly formed vortices have the great impact on the mixing of the ambient fluid with the jet fluid. These vortices interaction is the main reason for the transition of the flow to turbulent regime. Following figure shows the generation and growth of the vortices in the shear layer and flow transition from the laminar to turbulent.[2]

### 1.2.5 COHERENT STRUCTURES

Large scale turbulent fluid mass having phase correlated vorticity entirely over its spatial extent can be defined as the coherent structure. Alternately in the underlying 3D random vorticity fluctuations which are reason to characterize turbulence has a one vorticity component which is related to the phase all over its extent. Behaviour of these coherent structures in a jet is completely relying on the initial conditions. By using the acoustic excitations it is possible for us to find the frequency of formations for these structures. The advanced fundamental mode improves the flow such that it destroys the mechanism of the fine grained turbulence. Because of the viscous flow fine grained turbulence decreases downstream which then results in the amplification of the coherent structures. The coherent structure starts to grow in the highly unstable shear layer close to the nozzle tips. These structures continue to entrain the ambient fluid till 20 times the height of the nozzle.[2]

### 1.2.6 ASPECT RATIO

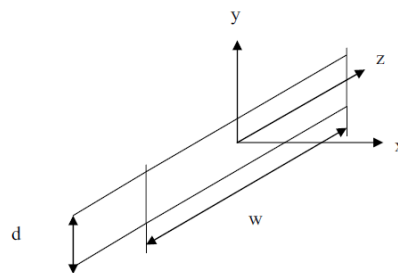


**Figure 3** Aspect ratio of a rectangular jet nozzle[5]

The jet aspect ratio is influential factor in case of the non-circular jets which impacts on the phenomenon like axis switching and evolution of the jet around the axis. The ratio of major axis to minor axis is defined as the aspect ratio in case of the rectangular jets. The flow is



found to be statistically two dimensional and free from the effect of the side walls when measured in the centre plane this is the result of having high aspect ratio.[5]

### 1.3 VORTICITY

Vorticity can be defined as a vector field which gives a microscopic measure of the rotation at any particular point in the fluid. The characterization of the vortices can be done using the parameters like distribution of velocity, circulation, the curl of flow velocity. It is clearly seen that the fluid velocity is greatest close to its axis and decreases as we go away from the axis.

In the initial phases of the jet development the next to nozzle a shear layer is formed between the jet and surroundings. Beyond the development stage of the jet in the nonlinear Kelvin-Helmholtz instability regime large scale vortices tend to roll up. This behaviour of dynamic formation and merging become identity of the transitional shear flow regime.[6]

#### 1.3.1 VORTEX DETECTION

In general terms the vortices are generated because of the phenomenon known as conservation of angular momentum. The characteristics of the vortices can be its location, circulation, core radius, drift velocity, peak vorticity, maximum circumferential velocity. During the convective flow generally the vortices are hidden because of the dominating nature of the fluid velocity. On the other hand streamline gives good indication of vortical structures. This can be seen from the fig shown below.

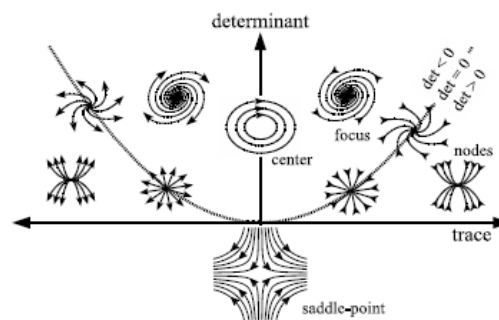


**Figure 4** Behaviour of autonomous ordinary differential equations of two degrees of freedom in different regions dependent on trace and determinant of the velocity gradient tensor given in equation.[7]





The vortex obtained from the gradient tensor indicates the vortices in the flow irrespective of the frame of reference. Following vortices appear in above figure for non-real Eigen values of the gradient tensor.[7]

$$\mathcal{G} = \frac{dU}{dX} = \begin{pmatrix} \frac{\partial U}{\partial X} & \frac{\partial V}{\partial X} \\ \frac{\partial U}{\partial Y} & \frac{\partial V}{\partial Y} \end{pmatrix} \quad (1.5)$$

The discriminant  $\lambda_2$  of non-real eigenvalues of the velocity tensor  $\mathcal{G}$  separates vortices from other patterns.

$$\begin{aligned} \lambda_2 &= (\text{trace } \mathcal{G})^2 - 4 \det(\mathcal{G}) \\ &= \left( \frac{\partial U}{\partial X} + \frac{\partial V}{\partial Y} \right)^2 - 4 \left( \frac{\partial U}{\partial X} \cdot \frac{\partial V}{\partial Y} - \frac{\partial U}{\partial Y} \cdot \frac{\partial V}{\partial X} \right) \end{aligned} \quad (1.6)$$

Negative values of  $\lambda_2$  are the indication of the vortices. In this  $\lambda_2$  generally does not consider boundary layers and shear layers as vortices. But the drawback with this is it does not provide any kind of information about the direction of rotation. This can be easily obtained by analysing the surrounding velocity field. [7]



## 2 INTRODUCTION TO PARTICLE IMAGE VELOCIMETRY (PIV)

### 2.1 PHYSICAL AND TECHNICAL BACKGROUND

Observing the nature is the most interesting part of human behaviour and also is of utmost importance for human survival. One can easily imagine how the observation of moving objects has evolved from first simple experiments with setups and tools easily available in nature. Today the same primitive behaviour becomes obvious, when small children throw little pieces of stone in a river and observe them floating downstream of the river. Such type of experimental arrangement allows us to make a rough estimation of the velocity of flowing water and to detect fluidic phenomenon such as swirls, wakes behind obstacles in the river, water shoots, etc.

As the investigation techniques evolved over the year's one of the great milestone during the evolution of techniques were achieved by Ludwig Prandtl, He promoted to replace the passive observation of the nature with planned experiments. These experiments were carefully planned to extract information about the flow utilizing visualization techniques. He carried out study aspects of unsteady separated flows behind wings and other objects by designing and utilizing flow visualization techniques in a water tunnel.[8]

### 2.2 PRINCIPLE OF PARTICLE IMAGE VELOCIMETRY (PIV)

In this flow investigation method the velocity vectors are derived from sub-sections of the target area of the particle seeded flow by measuring the movement of particles between two light pulses.

$$\Delta v = \frac{\Delta l}{\Delta t} \quad (2.1)$$

Where  $\Delta v$  the velocity of the component is,  $\Delta l$  is the particle displacement and  $\Delta t$  is the time between the two laser pulses.

The experimental setup of the PIV method consists of many sub systems. The seeded particle also called tracer particles are introduced in the flow. These particles are illuminated with the use of laser twice within very short time interval. Then the light scattered by the seeded



particles is recorded with camera. As described earlier the displacement of the particles is derived from the PIV recordings.

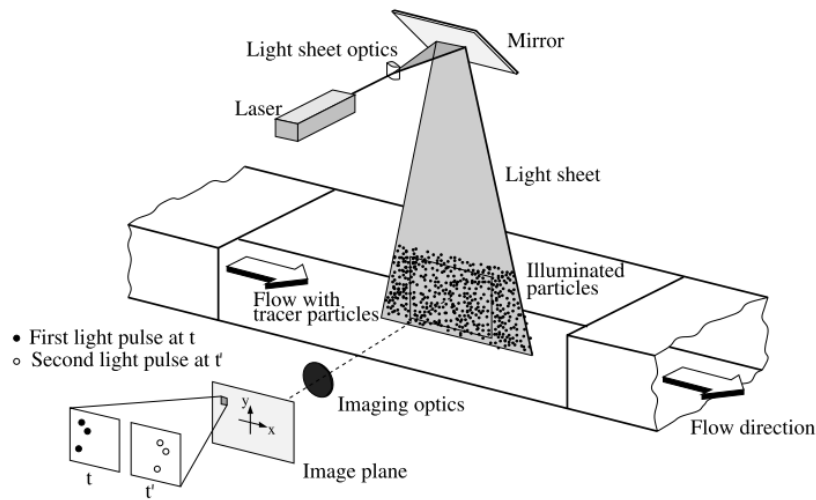


**Figure 5** General set up demonstrating PIV working principle [8]

The above figure shows PIV recording set up for the wind tunnel briefly sketches a typical setup for PIV recording in a wind tunnel. Tracer particles are added to the flow. A light sheet is illuminated twice by means of a laser. The particles follow local flow velocity between the two laser pulses. The light scattered by the particles is recorded with high quality lens either on a single frame (e.g. on a high-resolution digital or film camera) or on two separate frames on special cross-correlation digital cameras. After recording the images are divided into small subsections called interrogation area. Further the interrogation areas are cross correlated. The signal peaks are received for the cross correlation of the signal. The velocity vector field can be obtained by repeating this process over each recorded interrogation area.[3]

## 2.3 SOME GENERAL ASPECTS OF THE PIV METHOD

- Non-intrusive velocity measurement

Unlike other techniques the PIV is non-intrusive method i.e. the PIV is non-contact method which provides it edge over the other available velocity measuring techniques. This allows the application of PIV even in high-speed flows with shocks where the flow may be disturbed by the presence of the probes.

- Indirect velocity measurement



PIV technique measures the velocity of a fluid indirectly by means of the measurement of the velocity of tracer particles within the flow, in most of the applications the tracer particles are introduced in the flow before the experiment begins. In case of two phase flows there is no need for the introduction of the tracer particles as particles are already present in the flow. Interestingly, it is possible to measure the velocity of the particles themselves as well as the velocity of the fluid.

- Whole field technique.

PIV is a technique which allows recording images of large parts of flow fields in a variety of applications and also retrieving the accurate velocity information from these recordings. Aside from Doppler Global Velocimetry which is a new technique particularly appropriate for medium to high-speed air flow all other techniques for velocity measurements only allow the measurement of the velocity of the flow at a single point. Instantaneous image capturing and high spatial resolution of PIV allows the detection of spatial structures steady as well as in unsteady flow fields.

- Velocity lags.

As the tracer particles are introduced for the measurement of the flow velocity leads us to check carefully whether the particles will faithfully follow the motion of the fluid elements, Small particles shows better results in this aspect as compared to the larger particles.

- Illumination.

In case of the gas fluids the smaller particles demand high laser intensity in order to get the sufficient scattering light for capturing the PIV recordings. As the scattering efficiency of the particles increase with the size of the particles. This in fact contradicts the phenomenon of velocity lag discussed above. So in such condition the compromise has to be identified.[9]

- Duration of illumination pulse.

The duration of the illumination of light pulse is the critical aspect in the PIV recording. It should be short and sufficient enough to trace the particles motion. Error in the duration of pulse illumination can lead us to blurring of the image. The time



delay between the illumination pulses must be long enough to be able to determine the displacement between the images of the tracer particles and short enough to avoid particles to leave the interrogation area.

- Distribution of tracer particles in the flow.

For PIV a homogeneous distribution of medium density is desired for obtaining high quality PIV recordings. No structures of the flow field can be detected on a PIV recording of high quality.

- Density of tracer particle images.

There are three different types of image density can be identified which is illustrated in figure 6. In the case of low image density (figure 6.a), the images of individual particles can be detected and images corresponding to the same particle originating from different illuminations can be identified. In the case of medium image density (figure 6.b), the images of individual particles can be detected as well.

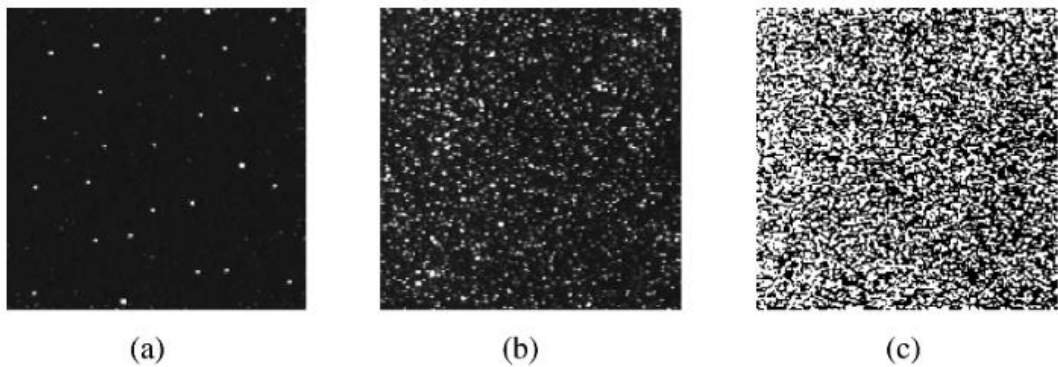


**Figure 6** The three modes of particle image density: a) low (PTV), b) medium (PIV), and c) high image density (LSV). [8]

In the case of high image density (figure 6.c), it is not even possible to detect individual images as they overlap in most cases and form speckles. This situation is called “Laser Speckle Velocimetry” (LSV)

- Number of components of the velocity vector.

Due to the planar illumination of the flow field only planar components of the velocity vector can be determined in standard PIV (2C-PIV). Methods are available to





extract the third component of the velocity vector as well (stereo techniques, dual-plane PIV and holographic recording) which is labelled as 3C-PIV.

- Temporal resolution.

Almost all of the PIV systems available provide to record at high spatial resolution but comparatively lower frame rates.

- Spatial resolution.

The size of the interrogation areas during evaluation must be small enough for the velocity gradients not to have influence on the results.

- Repeatability of evaluation.

PIV recordings can easily be exchanged for evaluation and post-processing with others different techniques. The information about the flow velocity field completely contained in the PIV recording can be used in different without the need to repeat the experiment.[8]

## 2.4 PIV COMPONENTS

### 2.4.1 TRACER PARTICLES

The tracer particle plays crucial role in the PIV recordings and has significant impact on the PIV results. It is necessary to go through the fluid mechanic properties of the tracer particles.

A primary source of error is if the densities of the fluid  $\rho$  and the tracer particles  $\rho_p$  do not match. Gravitationally induced velocity  $U_g$  can be derived from Stokes' drag law in for detecting the particle's behaviour under acceleration. Hence, we assume spherical particles in a viscous fluid at a very low Reynolds number. This gives

$$U_g = d_p^2 \frac{(\rho_p - \rho)}{18\mu} g \quad (2.2)$$

E.g.  $g$  is the acceleration due to gravity,  $\mu$  the dynamic viscosity of the fluid and  $d_p$  is the diameter of the particle. In analogy to equation (2.1), we can derive an estimate for the velocity lag of a particle in a continuously accelerating fluid.



$$U_s = U_p - U = d_p^2 \frac{(\rho_p - \rho)}{18\mu} a \quad (2.3)$$

Where  $U_p$  is the particle velocity. The step response of  $U_p$  typically follows an exponential law if the density of the particle is much greater than the fluid density:

$$U_p(t) = U \left[ 1 - \exp\left(-\frac{t}{\tau_s}\right) \right] \quad (2.4)$$

With the relaxation time  $\tau_s$  given by

$$\tau_s = d_p^2 \frac{\rho_p}{18\mu} \left( \cong \frac{d^2}{\nu} \right) \quad (2.5)$$

While working with liquids in PIV the density mismatch problem is not that severe solid particles with adequate fluid mechanical properties can often be found. The problems regarding the use of PIV in gaseous medium are similar to the Laser Doppler Velocimetry. As derived from the above equation the compromise has to be made between the particle size and light scattering properties.[10]

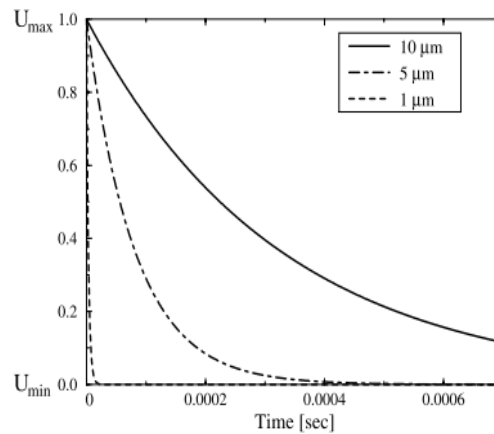


**Figure 7** Time response of oil particles with different diameters in a decelerating air flow[10]

## 2.4.2 LIGHT SCATTERING BEHAVIOUR

It is evident from the various researches that the quality of the PIV recording entirely depends upon the scattered light power. Also it is recommended to select the proper particle size instead of increasing the laser power. It can be said that the light scattered by small particles is a function of the ratio of the refractive index of the particles to that of the surrounding



medium, the particles size their shape and orientation. There are few other parameters like polarization and observation angle on which the scattering is dependant.[11]

Polar distribution of the scattered light intensity for oil particles of different diameters in air with a wavelength  $\lambda$  of 532 nm according to Mie's theory.

$$q = \frac{\pi d_p}{\lambda} \quad (2.6)$$

If  $q$  is larger than unity, approximately  $q$  local maxima appear in the angular distribution over the range from  $0^\circ$  to  $180^\circ$

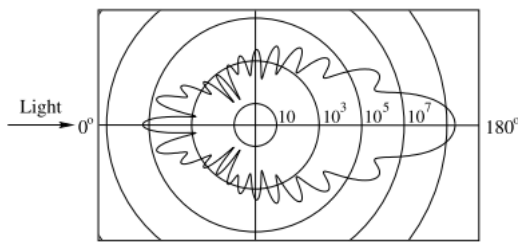


**Figure 8** Light scattering by a  $1\mu\text{m}$  oil particle in Air [11]

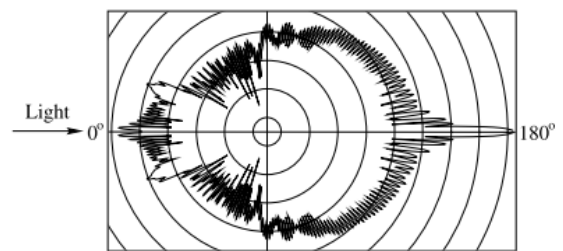


**Figure 9** Light scattering by  $10\mu\text{m}$  oil particle in Air [11]

Sr No.	Type	Material	Mean Diameter
1.	Solid	Polystyrene	05-10
2	Solid	Alumina $\text{Al}_2\text{O}_3$	0.2-5
3	Solid	Titanium $\text{TiO}_2$	0.1-5
4	Solid	Glass micro-spheres	0.2-3
5	Solid	Glass micro-balloons	30-100
6	Solid	Granules for synthetic coatings	10-50
7	Solid	Diethylphthalate	1-10
8	Solid	Smoke	<1
9	Liquid	Different oils	0.5-10
10.	Liquid	Di-ethyl-hexyl-sebacate (DEHS)	0.5-1.5
11.	Liquid	Helium filled soap bubbles	1000-3000

**Table 1** Seeding materials for gas flows [11]



### 2.4.3 GENERATION OF PARTICLE

Seeding of liquids is easy compared to the seeding in gases. In case of liquid it is even possible that you don't have to seed particles externally. Usually, the particles are added to the liquid and mixed to obtain homogenous phase.

Sr No.	Type	Material	Mean Diameter
1.	Solid	Polystyrene	10-100
2	Solid	Aluminium flakes	2-7
3	Solid	Hollow glass spheres	10-100
4	Solid	Granules for synthetic coatings	10-500
5	Liquid	Different oils	50-500
6.	Gaseous	Oxygen bubbles	50-1000

**Table 2** Seeding materials for liquid flows [11]

In gases, if the density of the particles is not accurate enough this may lead us to velocity lag. In case of open experiment setup, seeding particles used should be non-hazardous for the health as there is possibility of the inhaling of the seeding particles by the experimentalist. Sometimes the particles must be injected into the flow shortly before the gaseous medium enters the test section. While injecting the particles there should be no disturbance to the main flow and also it should be done in a way that the resulting tracer structure becomes homogenous.[12]

### 2.4.4 OIL DROPLET SEEDING OF AIR FLOW

Oil being non-hazardous has advantage over the other seeding particles. Also stay in the air for longer time with maintaining their size under various conditions.

The aerosol generator consists of a closed cylindrical container having two air inlets and one aerosol outlet. Four air supply pipes mounted at the top and dip into vegetable oil inside the container. They are connected to one air inlet by a tube and each has a valve. The pipes are closed at their lower ends (see figure 2.10). Four Laskin nozzles each having 1mm in diameter are equally spaced on the periphery of each pipe.[13]



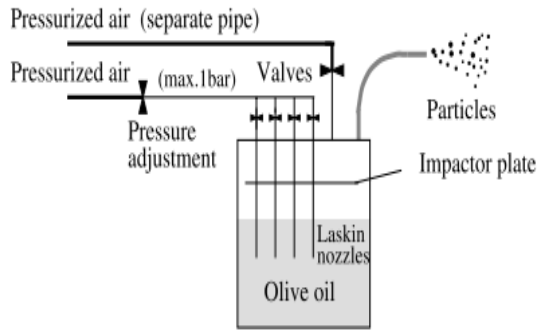


**Figure 10** Seeding particle generator [8]

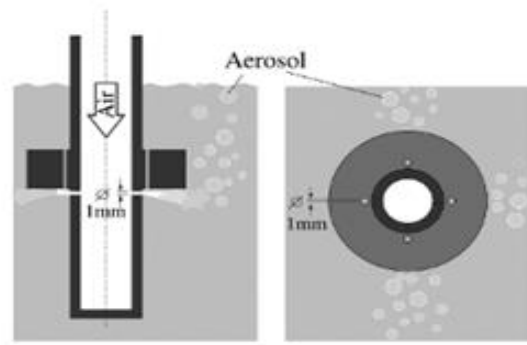


**Figure 11** Sketch of Laskin Nozzle [8]

A horizontal circular impactor plate is placed inside the container, and small gap of about 2mm is formed between the plate and the inner wall of the container. The second air inlet and the aerosol outlet are connected directly to the top. Two pressure gauges are used on the inlet of the nozzles and inside the container. Compressed air with 0.5 to 1.5 bar pressure difference with respect to the outlet pressure is supplied to the Laskin nozzles. This creates air bubbles within the liquid. Due to the shear stress induced by the tiny sonic jets, small droplets are generated and carried inside the bubbles towards the oil surface. Big particles are retained by the impactor plate; small particles escape through the gap and reach the aerosol outlet. The number of particles can be controlled by the four valves at the nozzle inlets. The size of the particle depends on the type of liquid used and the external pressure applied.[8]

## 2.4.5 LIGHT SOURCES

### LASERS

Lasers are widely used in PIV, because of their ability to emit monochromatic light with high energy density, which can easily be bundled into thin light sheets for illuminating and recording the tracer particles.

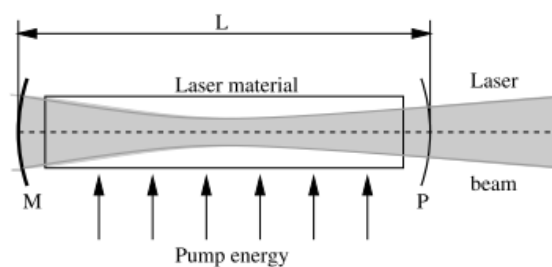


**Figure 12** Schematic Diagram of laser [11]





There are three main components in the laser

- The laser material
- The pump source
- The mirror arrangement

Quantum mechanics tell us that each atom can be brought to different kind of state. During the jump to higher energy state the atom has to be given energy and on the contrary when the atom jumps back to lower energy state it emits the energy in the form of photons and which also can be formulated as  $E_2 - E_1 = h\nu$ . This process of emitting photon to jump to enter the lower energy state is called spontaneous emission. In the other case incident photon can stimulate an atom in the excited  $E_2$  state into a specific, non-spontaneous, transition to  $E_1$ . Then total two photons are emitted. The impinging wave therefore is coherently amplified (stimulated emission)

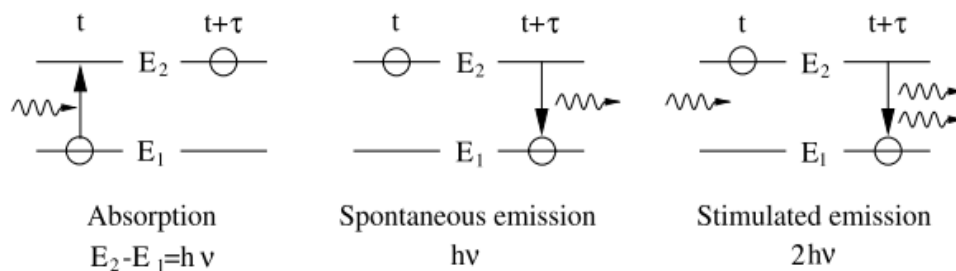


**Figure 13** Elementary kinds of interactions between atoms and electromagnetic radiation [11]

In case of population density inversion for which condition is  $N_2 > N_1$  [atoms/m<sup>3</sup>], stimulated emission takes place but in case of  $N_1 > N_2$ , absorption is occurred. For the working of laser population inversion should take place. The external energy has to be supplied as the atoms in the Laser material are in the ground energy state. The external energy source can be pump mechanism which can be selected on the basis of the laser material. Solid laser materials are generally pumped by electromagnetic radiation, semiconductor lasers by electronic current, and gas lasers by collision of the atoms or molecules with electrons and ions. Solid laser materials are generally pumped by electromagnetic radiation, semiconductor lasers by electronic current, and gas lasers by collision of the atoms or molecules with electrons and ions. [11]



The problem with two energy level system is when number of atoms  $N_2$  in level  $E_2$  equals the number in level  $E_1$  there is equal possibility of absorption and stimulated emission. Hence at least system with 3 energy state is required for population inversion to take place. As a consequence of population inversion through energy transfer by external energy source like pump mechanism spontaneous emission occurs in all possible directions which cause excitation of further neighbouring atoms. This initiates a rapid increase of stimulated emission and therefore of radiation in a chain reaction. Rapid stimulated emission takes place because of chain reaction.

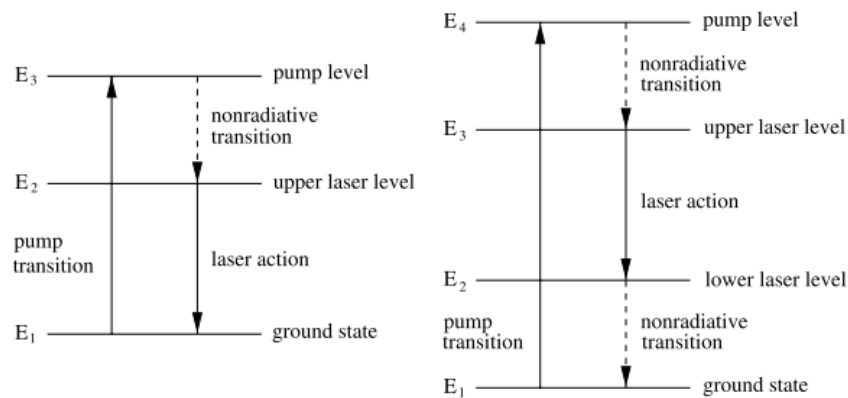


**Fig. 2.1** Level diagrams of three (left) and four (right) level lasers [11]

Neodym-YAG lasers (Nd:YAG lasers  $\lambda = 1064 \text{ nm}$  and  $\lambda = 532 \text{ nm}$ )

are the most important solid-state laser for PIV in which the beam is generated by  $\text{Nd}^{3+}$  ions. The  $\text{Nd}^{3+}$  ion can be incorporated into various host materials. For laser applications, YAG crystals (yttrium-aluminium-garnet) are commonly used. Nd:YAG lasers have a high amplification and good mechanical and thermal properties. Excitation is achieved by optical pumping in broad energy bands and non-radiative transitions into the upper laser level. Solid-state lasers can be pumped with white light as a result of the arrangement of the atoms which form a lattice. The periodic arrangement leads to energy bands formed by the upper energy levels of the single atoms. Therefore, the upper energy levels of the system are not discrete as in the case of single atoms, but are continuous.

As already mentioned, the Nd: YAG laser is a four-level system and has comparably low laser threshold. At standard operating temperatures the Nd: YAG laser emits the wavelength of  $1064 \text{ nm}$ . During the relaxation mode as the threshold is reached population inversion takes place. Design of the laser cavity is the deciding factor for the threshold value. In this pattern, we will likely have many successive laser pulses obtained during the pump pulse of



the flash lamp. Inclusion of the quality switch (Q-switch) inside the cavity gives the option to operate the laser in the triggered mode.[8]

The Q-switch has the effect of altering the resonance characteristics of the optical cavity. If the Q-switch is operated, allowing the cavity to resonate at the most energetic point during the flash lamp cycle, a very powerful laser pulse, the giant pulse, can be achieved. Q-switches normally consist of a polarizer and a Pockels cell. The Q-switched mode is mostly favoured in the use of PIV. PIV lasers are mostly designed as double oscillator systems. This enables the user to adjust the separation time between the two illuminations of the tracer particles independently of the pulse strength. The beam of Q-switch lasers is linearly polarized. For PIV, and many other applications, the fundamental wavelength of 1064nm is frequency-doubled using special crystals. After separation of the frequency-doubled portion, approximately one third of the original light energy is available at 532 nm. Nd:YAG lasers are usually driven in a repetitive mode. [8]

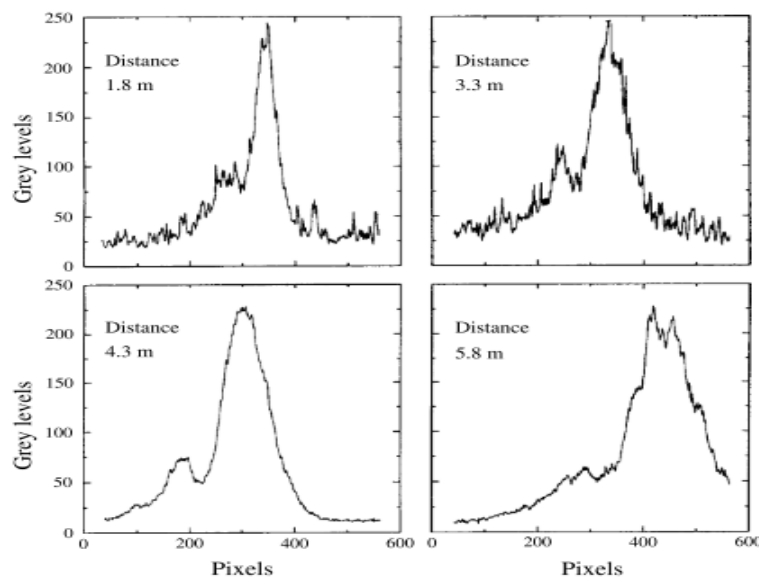


**Figure 14** Evolution of the light sheet profile with increasing distance from the laser [8]

## 2.5 PIV RECORDING TECHNIQUES

The PIV recording can be done by or can be classified in two different methods: single frame/multi-exposure PIV (figure 4.1) and multi-frame/single exposure. The main difference between the two methods is that single frame /multi exposure PIV does not retain information on their temporal order of the illumination pulse. This gives rise to directional ambiguity in the



recovered displacement vector. Methods like image shifting, pulse tagging are introduced to account for directional ambiguity.

In contrast, multi-frame/single exposure PIV recording inherently preserves the temporal order of the particle images. Even in terms of evaluation this approach is much easier to handle.

### 2.5.1 SINGLE FRAME/MULTI-EXPOSURE RECORDING

When using single frame multi exposure recording two or more exposures of the same particles is stored on a single recording. As the both exposure are on same recording it is difficult to find out the first and the last exposure i.e it is impossible for us to get the direction of the particle.

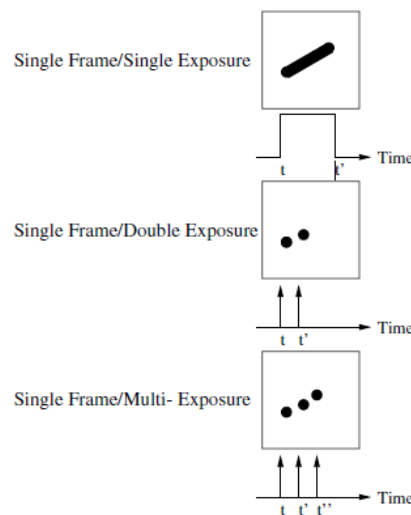


**Figure 15** *Single frame techniques* [14]

### GENERAL ASPECTS OF IMAGE SHIFTING

This is one of the method used for the removing the directional ambiguity obtained from the PIV recording. The method implies the constant additional displacement on the image of all tracer particles at the time of second illumination. Unlike other ambiguity removing techniques image shifting doesn't have to adopt the special method of the evaluation.

The figure shown below has two particles travelling in opposite direction. In this method we add additional shift,  $d_{\text{shift}}$  to the particle displacement  $d_1$  and  $d_2$ .



## ELIMINATION OF THE AMBIGUITY OF DIRECTION

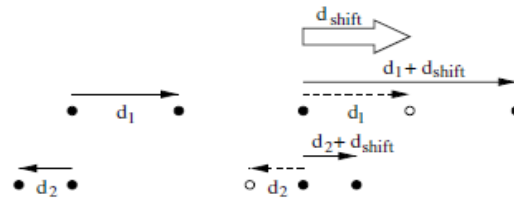


**Figure 16** Elimination of the ambiguity of direction of the displacement vector as observed in the recording plane [8]

But the selection of the additional shift is important and it has to be always greater than the maximum value of the reverse-flow component. The reason for this to keep the net displacement “Positive”. The elimination of the directional ambiguity does not depend on the direction within the observation plane where the shift takes place if the maximum of the corresponding reverse-flow component is predicted accordingly. Thus, an unambiguous determination of the sign of the displacement vector is established. The value and correct sign for the displacement vectors  $d_1$  and  $d_2$  will be obtained by subtracting the artificial” contribution  $d_{shift}$  after the extraction of the displacement vectors for the PIV recording.[3]

### 2.5.2 DOUBLE FRAME/MULTI-EXPOSURE RECORDING

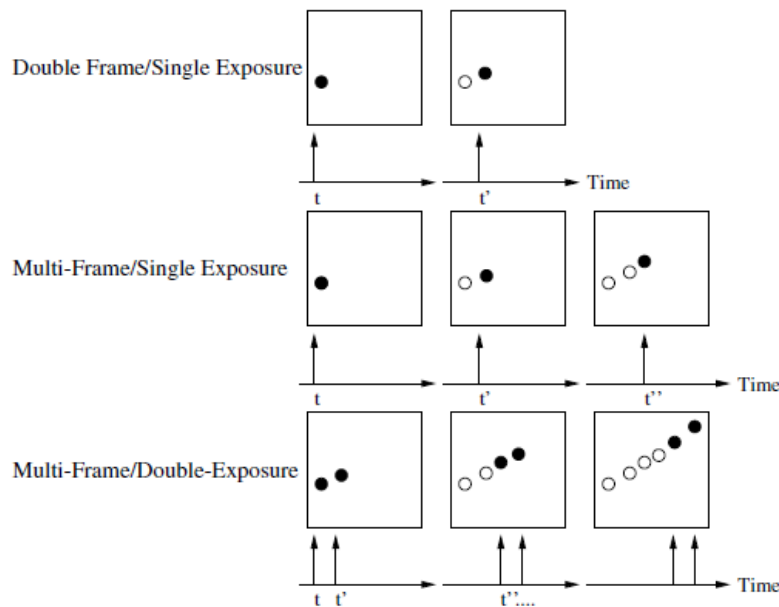


**Figure 17** Multiple frame techniques (open circles indicate the particles positions in the previous frames.)[15]

In this method the separation of the light of the different recordings on different frames provides us the advantages like particle direction clarity, allows the adaptation of the pulse separation time with wider range and also for the same interrogation window size we get the



higher signal to noise ratio. These higher ratios provide us to calculate the displacement in the smaller interrogation window size. In other words it can be said like it improves the results by enhancing the spatial resolution.

Separation of the different exposure needs to be carried out. This can be performed by the timing of the image recording with respect to the illumination. For example, by using high speed film cameras in sync with the copper vapour lasers or multiple oscillators Nd: YAG lasers.[15]

## 2.6 IMAGE EVALUATION METHOD FOR PIV

Most of the PIV realization is having similar approach in which the basic ground for them is digitally performed Fourier algorithm. But there are still some optical methods which are necessary for understanding the available set up. Displacement can be derived from the PIV recordings using certain type of interrogation scheme on the recording. Initially this process was carried out manually but thanks to computers and modern image processing techniques which made this process easy.

The application of tracking methods that is to follow the images of an individual tracer particle from exposure to exposure is advisable only in case of the low image density.

Actually in case of the PIV vector maps the images with higher density are preferred .The higher density PIV vector maps also can be used for the comparison between the experimental data and numerically simulated data. This demand requires a medium concentration of the images of the tracer particles in the PIV recording. In the medium concentration matching pairs of the particles cannot be detected by simple visual inspection. So, this draw back has to overcome by using statistical approach. This statistical approach has to be followed by the tracking algorithm. This will provide sub window spatial resolution of the measurement this is also known as super resolution PIV.[16]

Following figure shows the flow chart of the fully digital auto correlation method.



**Figure 18** Analysis of single frame/double exposure recordings the fully digital autocorrelations method [16]



During the analysis sampling is performed on the PIV recordings. In these PIV recordings small interrogation windows are considered for sampling process and typically with 20-50 samples in every dimension. For each sampled window auto correlation is carried out and definite position of the peak is determined. Calculation of the auto correlation function can be done in the two types firstly in the spatial domain or the bypass over the frequency plane through the use of FFT algorithms.

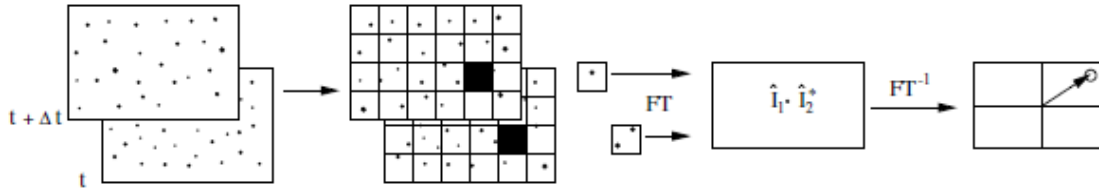


**Figure 19** Analysis of double frame/single exposure recordings: the digital cross correlation method [16]

The above figure shows the general procedure when the double frame single exposure is carried out. Cross correlation between two interrogation windows sampled from the two recordings is calculated. It would be beneficial to offset both these samples depending upon the mean displacement of the tracer particles between the intervals of the two illuminations. This helps in providing better result by reducing in plane loss of correlation. This increases the correlation peak strength. These calculations are further carried out with FFT algorithms.

Even for the case of single frame double exposure it is possible to use the cross correlation technique. The changes which are needed to be done are the slight displacement of the interrogation of the windows from each other and also selecting the higher interrogation window size. By implementing these changes the process can compensate for the in plane losses.



**Figure 20** Analysis of single frame/double exposure cross correlation method [16]

Auto correlation of the system can also be obtained by employing optical Fourier transform. For obtaining the auto correlation function a set up with two optical Fourier processors has to be used. A spatial light modulator is required to store the output from the first Fourier



processor. There are no optical means which are reliable to provide the 2D cross correlation function for PIV.

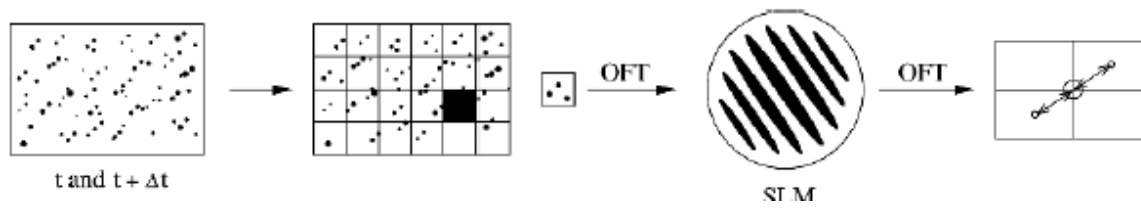


**Figure 21** Analysis of single frame/double exposure recordings: the fully optical method [16]

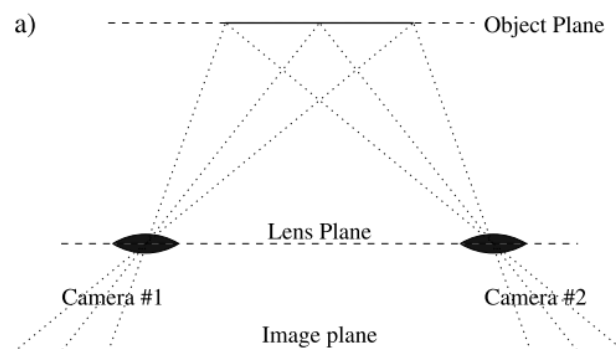




## 2.7 STEREO PIV

Use of the two cameras for getting the perception of the 3D i.e. depth has been performed in the engineering field since several decades. Interestingly this phenomenon of having the 3D dimension Perception has the close resemblance with the binocular, which we use to distinguish between the object which are far and near to us. The out of plane component in this case the 3 velocity component is projected on to the object plane and causes the perspective error in the plane component. When we are measuring particle displacement in all three dimensions. We can consider this situation as 3 unknowns along the three co-ordinates  $x, y, z$  providing us only 3 single views with two equations. By adding the other views provide us with two different equations which we can use for solving 3D information. Human body follows the same procedure in which our eyes records two Single views and our brain combines these to get the 3D dimension vision in the real time.[17]

As the opening angle between the cameras reaches close to  $90^\circ$  gives us advantage of measuring the out of plane component with much more higher precision. Due to the experimental limitations it is not possible to always have the both cameras at the same base. To overcome such practical limitations. The solution in which symmetrical arrangement of the cameras can be replaced with asymmetrical recording and similar calibration methods has been found. Also due to use of the imaging lenses with large focal length creates new problem in the recording. These types of lenses have the limited angular aperture and this limits distance between the lenses in a translation imaging approach. These lenses also show the limitation by decreasing the modulation transfer function as we move toward the edges of field of view. It is necessary to have a good MTF at small  $f$  numbers for properly imaging the small particles. The best MTF can be obtained near the principal axis alternative angular displacement method (figure 7.1b) aligns the lens with the principal viewing direction.



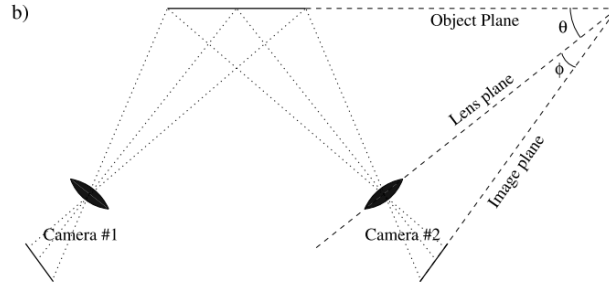


**Figure 22** Basic stereoscopic imaging configurations

*a) Lens translation method, b) angular lens displacement with tilted plane (Scheimpflug condition).[17]*

The need for small f-numbers can be achieved by following the Scheimpflug criterion in which image plane, lens plane and object plane for each of the cameras intersect in a common line. The Scheimpflug imaging arrangement increases the perspective distortion which in turn related to the oblique view of the arrangement.[17]

### 2.7.1 RECONSTRUCTION GEOMETRY

This section will emphasize on geometry which provides the 3 dimensional displacement value form the available two planar displacement fields. As discussed earlier the modern day usage of the asymmetrical approach to get more precise 3<sup>rd</sup> dimension. The cameras in this case can be placed in any desirable configuration (Only the arrangement should have non collinearity of the viewing axes).

$$x'_i - x_i = -M \left( D_x + D_z \frac{x'_i}{z_o} \right) \quad (2.7)$$

$$y'_i - y_i = -M \left( D_y + D_z \frac{y'_i}{z_o} \right) \quad (2.8)$$

In the following we will use the angle  $\alpha$  in the XZ plane between the Z axis and the ray from the tracer particle through the lens centre O to the recording plane as shown in figure 7.2.

Correspondingly,  $\beta$  defines the angle within the YZ plane.

$$\tan \alpha = \frac{x'_i}{z_o} \quad (2.9)$$

$$\tan \alpha = \frac{y'_i}{z_o} \quad (2.10)$$



The velocity components measured by the left camera are given by:

$$U_1 = \frac{x'_i - x_i}{M \Delta t} \quad (2.11)$$

$$V_1 = -\frac{y'_i - y_i}{M \Delta t} \quad (2.12)$$

The velocity components for the right camera  $U_2$  and  $V_2$  can be determined accordingly. Using the above equations, the three velocity components ( $U, V, W$ ) can be reconstructed from the four measured values. For  $\alpha, \beta \geq 0$  we obtain:

$$U = \left( \frac{U_1 \tan \alpha_2 + U_2 \tan \alpha_1}{\tan \alpha_1 + \tan \alpha_2} \right) \quad (2.13)$$

$$V = \left( \frac{V_1 \tan \beta_2 + V_2 \tan \beta_1}{\tan \beta_1 + \tan \beta_2} \right) \quad (2.14)$$

$$\begin{aligned} W &= \left( \frac{U_1 - U_2}{\tan \alpha_1 + \tan \alpha_2} \right) \\ &= \left( \frac{V_1 - V_2}{\tan \beta_1 + \tan \beta_2} \right) \end{aligned} \quad (2.15)$$

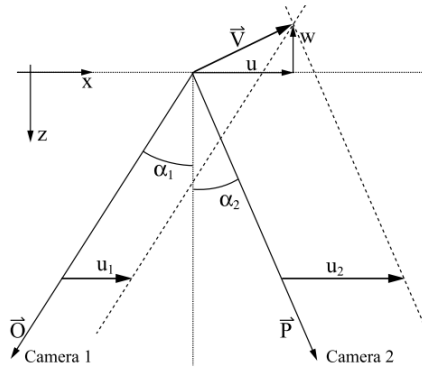


**Figure 23** Stereo viewing geometry in the XZ-plane [18]

These formulae are general and apply to any imaging geometry. Note, that there are three unknowns and four known measured values, which results in an over determined system that can be solved in a least-squares sense.



$$\begin{bmatrix} U_1 \\ V_1 \\ U_2 \\ V_2 \end{bmatrix} = \begin{bmatrix} 1 & 0 & -\frac{O_x}{O_z} \\ 0 & 1 & -\frac{O_y}{O_z} \\ 1 & 0 & -\frac{P_x}{P_z} \\ 0 & 1 & -\frac{P_y}{P_z} \end{bmatrix} \cdot \begin{bmatrix} U \\ V \\ W \end{bmatrix}$$

$$\mathbf{U}_{\text{meas}} = \mathbf{A} \cdot \mathbf{V}$$

$$\Rightarrow \mathbf{V} = (\mathbf{A}^T \cdot \mathbf{A})^{-1} \cdot \mathbf{A}^T \cdot \mathbf{U}_{\text{meas}}$$

The residuals  $\varepsilon_{\text{residual}}$  of this least squares fit can be used as a measure of quality for the three component measurement result. In practice residuals 0.1–0.5 pixel are common.[18]

## 2.7.2 STEREO VIEWING CALIBRATION

In order to reconstruct the local displacement vector the viewing direction and magnification factor for each camera must be known at each point in the respective images. This correspondence between the image (x, y) and the object plane (X,Y) may in fact be described through geometric optics; however, it requires exact knowledge of the imaging parameters such as the lens focal length, f, the angles between the various planes,  $\theta$ ,  $\phi$  (see figure 7.1b), the actual position of the lens plane (which is not simple to determine) and the nominal magnification factor,  $M_o$  (the magnification along the principal optical axis).[18]

The viewing direction and magnification vector for each camera is necessary to know at each point in the available images. This information further will be important to reconstruct the local displacement. Geometric optics helps us to find corresponding relation between image (x, y) and the object plane (X,Y). It is necessary for a person to know the imaging parameters such as lens focal length, f, the angles between the various planes,  $\theta$ ,  $\phi$  (see figure 7.1b), the actual position of the lens plane and the nominal magnification factor.

$$x = \frac{f x \sin \phi}{M_o \sin \theta (x \sin \phi + f M_o)} \quad (2.17)$$

$$x = \frac{f y}{x \sin \phi + f M_o}$$

For the reconstruction of the images, we implemented the projection equations based on perspective projection. Using homogeneous coordinates the perspective projection is expressed by:

$$\begin{bmatrix} \omega_o X \\ \omega_o Y \\ \omega_o \end{bmatrix} = \begin{bmatrix} a_{11} & a_{12} & a_{13} \\ a_{21} & a_{22} & a_{23} \\ a_{31} & a_{32} & a_{33} \end{bmatrix} \begin{bmatrix} \omega_i x \\ \omega_i y \\ \omega_i \end{bmatrix}$$



where  $\omega_o$  and  $\omega_i$  are constants and  $a_{33} = 1$ . When rewritten in standard coordinates the following two nonlinear expressions are obtained:

$$\begin{aligned} X &= \frac{a_{11}x + a_{12}y + a_{13}}{a_{31}x + a_{32}y + 1} \\ X &= \frac{a_{21}x + a_{22}y + a_{23}}{a_{31}x + a_{32}y + 1} \end{aligned} \quad (2.18)$$

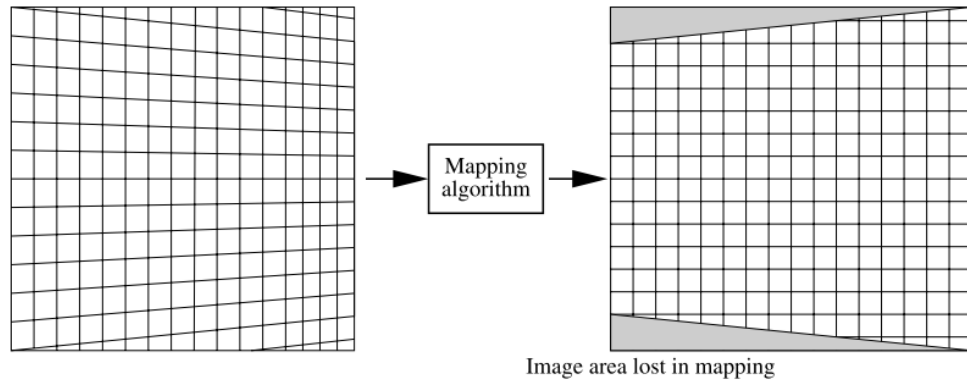


**Figure 24** The back-projection algorithm has to map the recorded image on the left to the reconstructed image on the right .[18]

The projection equations can be used to map recovered 2-C displacement data or entire images onto an object space that is common to both camera views. Due to the perspective distortion however the original raw image pixels can never be mapped at optimum sampling distances.[18]

### 2.7.3 CAMERA CALIBRATION

Along with the calibration procedure the information about the camera is also important for the reconstructing of the 3 dimensional velocity vector. As one of the approach is to measure the position of the cameras with respect to any known point in the calibration target. This calibration takes place by camera triangulation method.

It is quite difficult to perform camera triangulation when the measurement has to be proceeding from the distance. In order to recover the camera position there are two primary calibration solutions are developed. First solution is empirical oriented whereas the second one is based on the physical model. There is also third approach known as the self-calibration which is developed from the machine vision, this approach is now very popular in the tomographic PIV, micro PIV and stereoscopic PIV.[8]



A very general approach for calibrating the stereo PIV set up is using planar calibration targets which are placed over the light sheet. These calibration sheets consists of the grid which includes dots, crosses etc. This grid should be detected by means of the simple image processing techniques. A single image of planar calibration marks is then sufficient to calculate adequate mappings between image space and object space. But the problem with this method is it does not provide any information about the camera angles which is far more important in case of reconstruction of the three component displacement vector. This problem can further overcome by using multi-level calibration targets that have reference markers at different heights.[8]

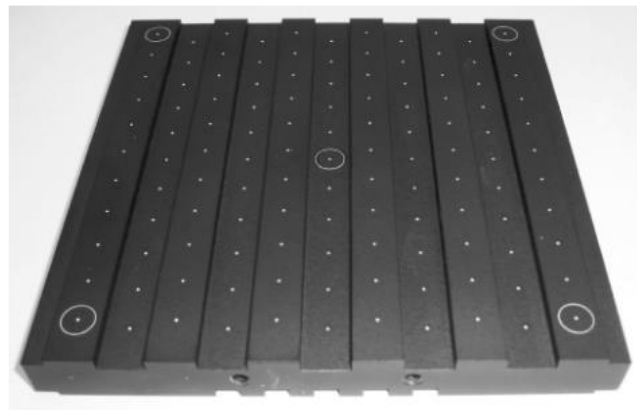


**Figure 25** Precision machined twin level calibration target with dot pattern for stereo PIV calibration. Levels are separated by 2 mm; dots are equally spaced on a 10mm grid. [8]

## 2.7.4 DISPARITY CORRECTION

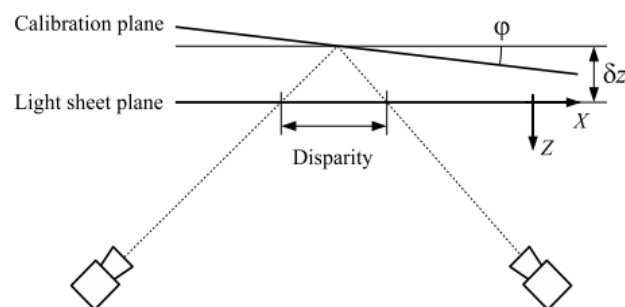


**Figure 26** Misalignment between calibration target and light sheet plane results in a mismatch between the actual imaged areas [19]



The reconstruction of the 3-C vector from two different 2-C PIV recordings can be done with proper information from the camera calibration. These 2-C PIV recordings are done at two different places and at different orientation. Reconstruction approach assumes that the calibration target is perfectly aligned with the centre of the light sheet plane. While experimenting this is difficult to achieve, in fact a slight out-of-plane position and minor rotation of the target can introduce a significant misalignment of imaged light sheet volumes.[19]

### 2.7.5 STEREOSCOPIC CONFIGURATION

Generally there are two configurations for stereoscopic PIV

- 1) Translation systems or lateral displacement
- 2) Rotational systems or angular displacement

#### Translational Systems

In this type of the configuration the camera axis is generally parallel to each other and perpendicular to the light sheet as shown in the figure below. In this case it is not necessary for the cameras to be symmetric to the system axis. This configuration is the simplest of the all available configurations.

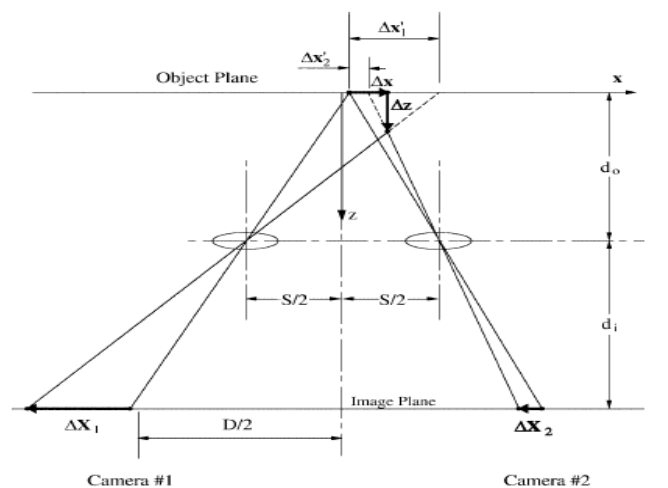


**Figure 27** Schematic of stereo camera in the translation configuration [20]

In this configuration the object plane, lens plane and image plane are all parallel to each other so image field has the uniform magnification. Also we can achieve good image focus without any changes to aperture as used in single camera PIV. Two image can be readily be super



imposed without additional manipulation. Spatial resolution will be same as the two individual views.

There is only small common area between both of the cameras. However, this common area can be maximized offsetting the frame away from the lens axis.

$$D = (1 + M_n) S \quad (2.19)$$

Where D is the distance between the sensors, S is the distance between the camera and lens axis. However, the vignetting caused by camera body makes off setting difficult.

Apart from this there is another problem with the translational configuration there is an upper bound to the off axis angle  $\theta$  subtended by the centre of the region of interest to the centre of the lens. This problem mainly arises from the design of the lens. Usually, lens performances are degraded when they are forced to operate on the outer limit of its specification. The relative error in the third component measurement is affected by the off-axis angle; this informs us that translation system has limited accuracy compared to the other configurations.[20]

The exact relationship between the original particle displacement and the apparent displacement measured by the camera can be given by the formulas given below.

$$\Delta Z = \frac{-d_o (\Delta X_1 - \Delta X_2)}{M_n S - (\Delta X_1 - \Delta X_2)} \quad (2.20)$$

$$\Delta x = \frac{\Delta X_1 \left(x - \frac{s}{2}\right) - \Delta X_2 \left(x + \frac{s}{2}\right)}{M_n S - (\Delta X_1 - \Delta X_2)} \quad (2.21)$$

$$\Delta Z = \frac{-y \Delta z}{d_o} + \frac{\Delta Y_1 + \Delta Y_2}{2 M_n} \left[ \frac{\Delta z}{d_o} - 1 \right] \quad (2.22)$$

## Rotational systems

In this configuration the restriction on the off axis angle  $\Theta$  is removed. Below schematic diagram shows the general arrangement of the configuration





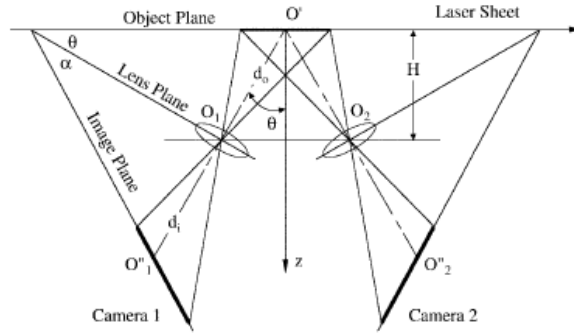
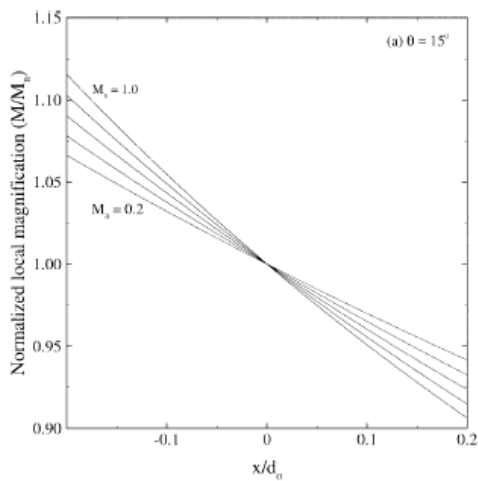


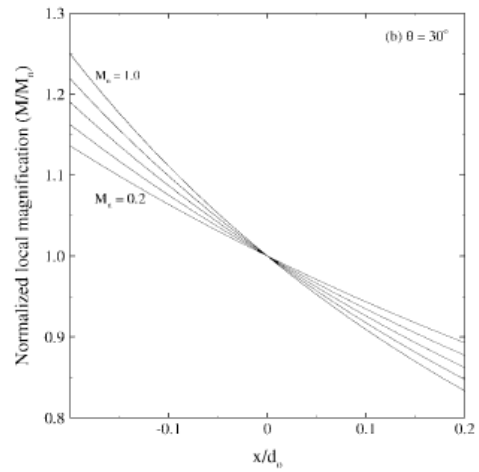
**Figure 28** Basic configuration for stereoscopic PIV systems: Angular-displacement method [20]

The important difference between both of the configuration can be clearly seen that the camera axes are no longer parallel to each other in fact they intersect object plane at the system axis. This provide the advantage that the now the angle  $\theta$  can be increased without hampering the lens performances. This gives us the more precise value of the out of plane component. As the camera axis is no longer parallel the magnification is no longer uniform over the field. Image plane is further rotated by an angle  $\alpha$  in order to make object plane, lens plane and image plane collinear. This specific requirement is known as Scheimpflug criterion. The Scheimpflug makes good focus on all available particles in the object field on the image plane.

Following figure shows the variation of the magnification across the object plane in the Scheimpflug experiment for off axis angles of a)  $15^\circ$  b)  $30^\circ$  c)  $45^\circ$  and  $M_n$  lies in the range of 0.2-1 (increment step 0.2).



(a)



(b)



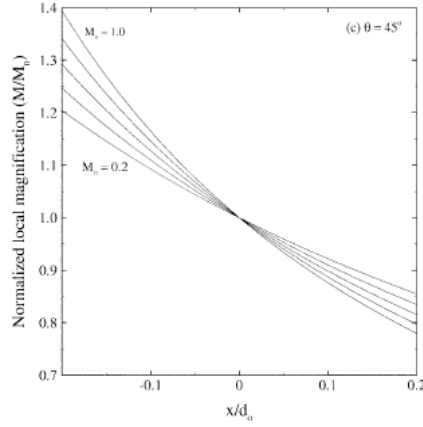


**Figure 29** Non-uniformity in magnification across the object plane in the Scheimpflug system for nominal magnifications varying between 0.2 and 1.0 in steps of 0.2: a)  $\theta = 15^\circ$ , b)  $\theta = 30^\circ$ , c)  $\theta = 45^\circ$  [20]

The distance in the horizontal axis in the object plane,  $x$ , is normalised by the nominal object distance  $d_0$  and the resulting local magnification is normalised by the nominal magnification. It appears that the non-uniformity increases with  $|x|$ ,  $\Theta$ ,  $M_n$ .

In the previous research variation of the Scheimpflug angular displacement system were developed in which the camera is placed on the either side of the light sheet. This arrangement benefited the experimenting in two ways. First, It was possible to use the both cameras in the forward scatter by properly orienting the direction of the laser beam. Secondly, the views are stretched identically.

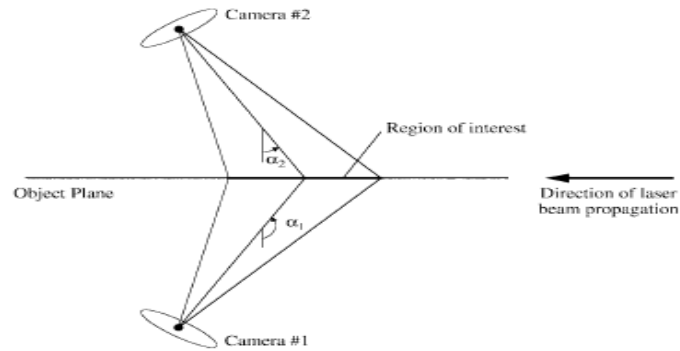


**Figure 30** Stereoscopic arrangement with camera on either side of the light sheet [20]

It is easily seen that the equation for the angular displacement system can be reduced to similar form to that of the translation system. Previous research has showed for system with Scheimpflug and non Scheimpflug system. [20]



## 2.8 TOMOGRAPHIC-PIV INTRODUCTION

### 2.8.1 INTRODUCTION TOMOGRAPHIC PARTICLE IMAGE VELOCIMETRY

The fluid research has been always interested in knowing the instantaneous 3D velocity field. As this provides the research an entire topology of unsteady coherent flow structures. 3 D velocity measurements are more relatable to the flow which is not symmetric about any plane or axis.

This method is based on the tomographic reconstruction of the 3D particle distribution. The recordings of the particle images from the illuminated volume are used to reconstruct 3D light intensity distribution and the particle images taken are taken from the various different angles. The two subsequent exposures of the particles images are obtained and by using 3D particle pattern cross-correlation instantaneous velocity measurement field can be obtained.

### 2.8.2 WORKING PRINCIPLE OF TOMOGRAPHIC-PIV

Schematic diagram shown below gives us idea of the general working principle of tomographic PIV.

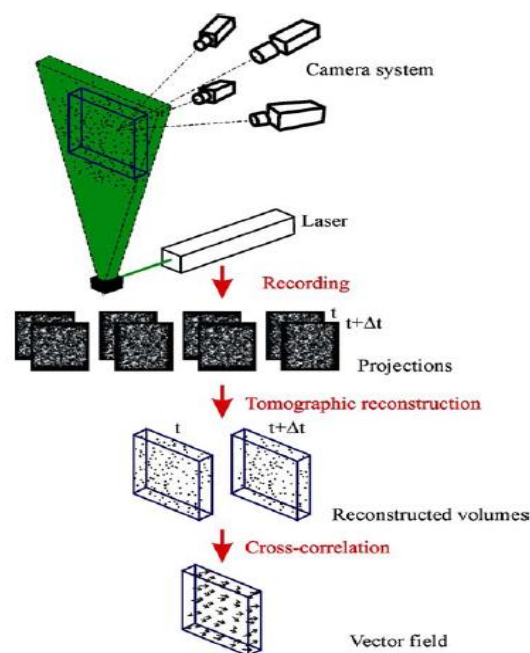


**Figure 31** Principle of tomographic – PIV [21]



The tracer particle introduced in the flow is illuminated by the pulsed laser beam. The light scattered from the particles is then recorded by using several CCD cameras at different orientation. The no of cameras used is in this is 4 unlike 2 in stereo PIV. As discussed earlier the Scheimpflug is used to focus the entire particles available in the volume image plane. The 3D particle distribution of the object is reconstructed using the 3D light intensity distribution from its projections on the CCD arrays in the experiment. Using 3D cross correlation the particle displacement within the selected interrogation volume can be obtained. This method have quiet similar calibration approach as like the stereo PIV. As the reason for calibration is to determine the relation between the image co-ordinates and the physical space.

During the calibration of the Tomo-PIV each and every camera records the images of the calibration target. This calibration procedure gives us the viewing directions and the field of the view. The tomographic reconstruction depends upon the quality of the triangulation done on the views of the different cameras. The mapping of the physical space with image coordinate system can be performed by any of two simple methods. First is camera pinhole model and second by a third-order polynomial in  $x$  and  $y$ . [21]

### **2.8.3 TOMOGRAPHIC RECONSTRUCTION ALGORITHM**

The tomographic PIV uses the optical tomography for the reconstruction purpose. Depending upon the properties of the measuring system it is possible to preselect a particular reconstructing method. In this reconstruction process initially particle distribution is discretely sampled on pixels from a small number of viewing directions. This also involves high spatial frequencies. In such condition the Algebraic reconstruction is methods are preferred compared to that of the analytical reconstruction methods.

### **2.8.4 ALGEBRAIC METHODS**

These method belongs to the category of the iterative method in which set of linear equations which are modelled to represent the imaging system are solved in the iterative manner. This method discretizes the particle distribution in the measurement volume as a 3D array of cubic voxel elements in  $(X, Y, Z)$  and intensity  $E(X, Y, Z)$ . These cubic voxel elements has the non-zero volume inside and zero value outside. The selection of the size is completely dependent



on the pixel size. Extension of the interrogation is carried out from pixel to voxel based by using cross correlation option. By projecting the light intensity distribution  $E(X, Y, Z)$  onto an image pixel  $(X_i, Y_i)$  we get returned value of pixel intensity  $(X_i, Y_i)$  and this pixel intensity can be represented in the form of a linear equation

$$\sum_{j \in N_i} w_{ij} E(X_j, Y_j, Z_j) = I(x_i, y_i) \quad (2.23)$$

Where  $N_i$  represents the voxels intercepted. The weighting coefficient  $w_{ij}$  explains the contribution of the  $j$ th voxel along with intensity  $E(X_j, Y_j, Z_j)$  to the pixel intensity  $I(x_i, y_i)$ . The weighting coefficient is calculated as the intersecting volume between the voxel and the line of sight (having the cross sectional area of the pixel) and which is normalized with the voxel volume.[22]

By application of the geometric optics the recorded pixel intensity can be represented as the object intensity  $E(X, Y, Z)$  and this intensity is integrated along the respective line of sight. The reconstructed particle is represented by a 3D Gaussian-type blob and as a diffraction spot projected in all the possible direction.

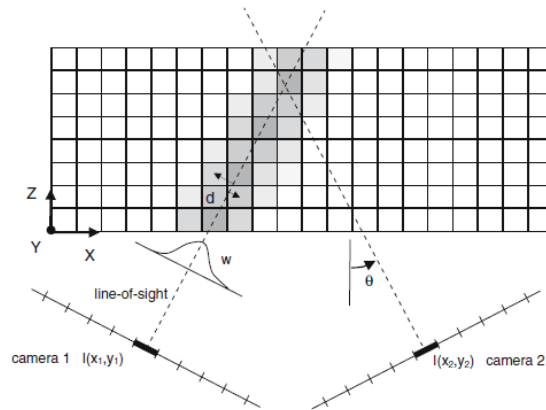


**Figure 32** Representation of the imaging model used for tomographic reconstruction. In this top-view the image plane is shown as a line of pixel elements and the measurement volume is a 2D array of voxels. The grey level indicates the value of the weighting coefficient in each of the voxel with respect to the pixel  $l(x_i, y_i)$  [22]

The following is the comparison carried out between ART (algebraic reconstruction technique) and MART (multiplicative algebraic reconstruction technique).

$$\text{ART} : E(X_j, Y_j, Z_j)^{k+1}$$

$$= E(X_j, Y_j, Z_j)^k + \mu \frac{I(x_i, y_i) - \sum_{j \in N_i} w_{ij} E(X_j, Y_j, Z_j)^k}{\sum_{j \in N_i} w_{ij}^2} w_{ij} \quad (2.24)$$



$$\begin{aligned}
\text{MART : } E(X_j, Y_j, Z_j)^{k+1} \\
= E(X_j, Y_j, Z_j)^k \left( \frac{I(x_i, y_i)}{\sum_{j \in N_i} E(X_j, Y_j, Z_j)^k} \right)^{\mu w_{ij}} \quad (2.25)
\end{aligned}$$

where  $\mu$  is a scalar relaxation parameter, which for ART is between 0 and 2 and for MART must be  $\leq 1$ . In ART method correction magnitude entirely depends on residual  $I(x_i, y_i) - \sum_{j \in N_i} w_{ij} E(X_j, Y_j, Z_j)$  and after that it is multiplied by a scaling factor and the weighting coefficient, this gives only the elements in  $E(X, Y, Z)$  affecting the  $i$ th pixel are updated. Whereas the MART follows the different method in which the magnitude of the update is obtained by the ratio of the measured pixel intensity  $I$  with the projection of the current object. Similarly like the ART the elements in the  $E(X, Y, Z)$  are updated. In addition to that the MART scheme requires that the value of the  $E$  and  $I$  are definite positive. [22]

## 2.9 PIV ERROR CORRECTION

As all of us are aware that the PIV is based on the statistical correlation of imaged sub regions to determine local flow velocities, it is subjected to some unwanted errors. The error can be because of finite tracer particle number, sample volume size and also image resolution. Sometimes these errors are easy to detect because they vary their behaviour depending upon the neighbouring vectors both in magnitude as well as in direction sense. Velocity vectors determined by correlating finite sub regions of tracer particle images are often biased. The reason for images taken being bias can be varying degrees by, out-of-boundary particle motion, correlations occurring between unmatched particle pairs, non-uniform particle distribution and variations in image intensity.

Currently the most widely used method used to eliminate the correlation error is to compare the vectors with their neighbouring vectors and check for any statistical or physical inconsistency shown by the vectors. This technique is purely based on the assumption that the correlation error vectors are far removed from the neighbouring vector in magnitude and in direction. But this error correction method only considers the most obvious correlation errors and completely unaware of the errors that severely limits the sub pixel accuracy and resolution.[23]



## **2.9.1 CORRELATION ERRORS**

Processing of the PIV recorded images is done by sub division into grid of overlapping windows. After that carrying out the auto correlation or cross correlation the vector for each window is found. Autocorrelation and cross-correlation generates a table having the correlation values over a range of displacement. Also the peak in the correlation table represents the overall displacement of the particles in the window. The error is mainly induced because of the insufficient data, poor quality of images from correlation anomalies resulting from unmatched tracer images within the correlated sample volume.

### **2.9.1.1 SEEDING DENSITY**

As the seeding particle density increases the probability of the finite region having same particle intensities and pattern decreases. This in fact increases the probability of the accurate measure of the displacement of a set of particles. In the previous researches it has been found that there drop in the spurious vectors in the PIV data if the number of particles within correlated region has been increased to near about ten particle images per region. Also the excess seeding can lead to insufficient illumination and can also hamper the characteristic of the flow being measured

### **2.9.1.2 INTERROGATION SIZE**

An alternative solution for this could be increasing the size of the sample volume. This will increase the number of particles per interrogation window. As the sample volume is increased, a smaller fraction of particles enter and exit relative to the total number of particles that remain within the sample volume between exposures. The research has shown significant errors due to an asymmetry in the peak correlation within the correlation table are associated with this phenomenon. Further solution for reducing these bias errors can be done by correlating with an interrogation window offset by the integer value of local particle pixel displacement. Using this method the out of boundary particle motion is significantly eliminated.

It has been concluded that the large velocity gradient are problematic as they generate the bias errors and also limits the maximum interrogation window size. This velocity gradient also can lead to unequal particle displacements causing the one part of interrogation window



to correlate with the different location than another part. The correlation table will show change instead of having one prominent peak for average displacement over the region it will show multiple peaks. As seen from the above discussed context there is a limit for seeding particle density and maximum interrogation window size. This limit severely restricts the use of the PIV.[23]

## 2.9.2 CORRELATION ERROR CORRECTION

The errors generated by the insufficient data and errors caused by the correlation anomalies can be easily eliminated. For elimination of such errors during processing the correlation table has to be multiplied with the table generated along the adjacent areas. The following image of the correlation table shows the example for this technique.

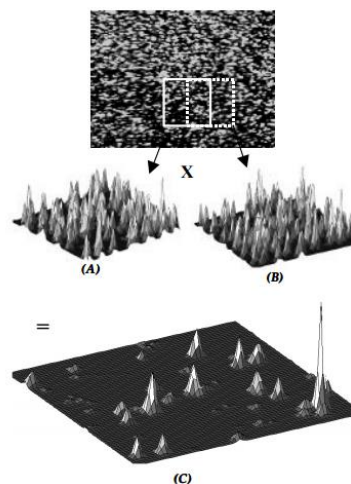


**Figure 33** Elimination of correlation anomalies by multiplying the correlation tables from adjacent regions. Correlation values that do not appear in both tables are eliminated allowing tracer particle displacement to be resolved. [23]

In the figure shown above the correlation table is multiplied with the adjacent correlation table with 50 % of the overlap. The resulting table has very low correlation anomalies. [23]

## 2.10 PIV UNCERTAINTY QUANTIFICATION

As PIV the use of PIV has been very largely increased this has attracted many of the researcher to find the various methods to quantify the uncertainties involved in the PIV measurement. By quantifying the measurement uncertainties will lead to use the PIV in greater extent and also good for PIV to find a place in the industrial applications as well. Previously these has been already estimated that the under normal experimental situations the





displacement error would be around 0.05 to 0.2 pixel. Recent research has shown the keen interest in specifying the uncertainty of each displacement vector in the interrogation area. There are many reasons which introduce the uncertainties in the PIV measurement.[24]

## 2.11 PIV ERROR SOURCES

As we know the error can be classified under two broader groups. Firstly random error and systematic bias error. Previous researches have advised us to rectify the systematic process as art of the processing whereas the random error can be dealt later.

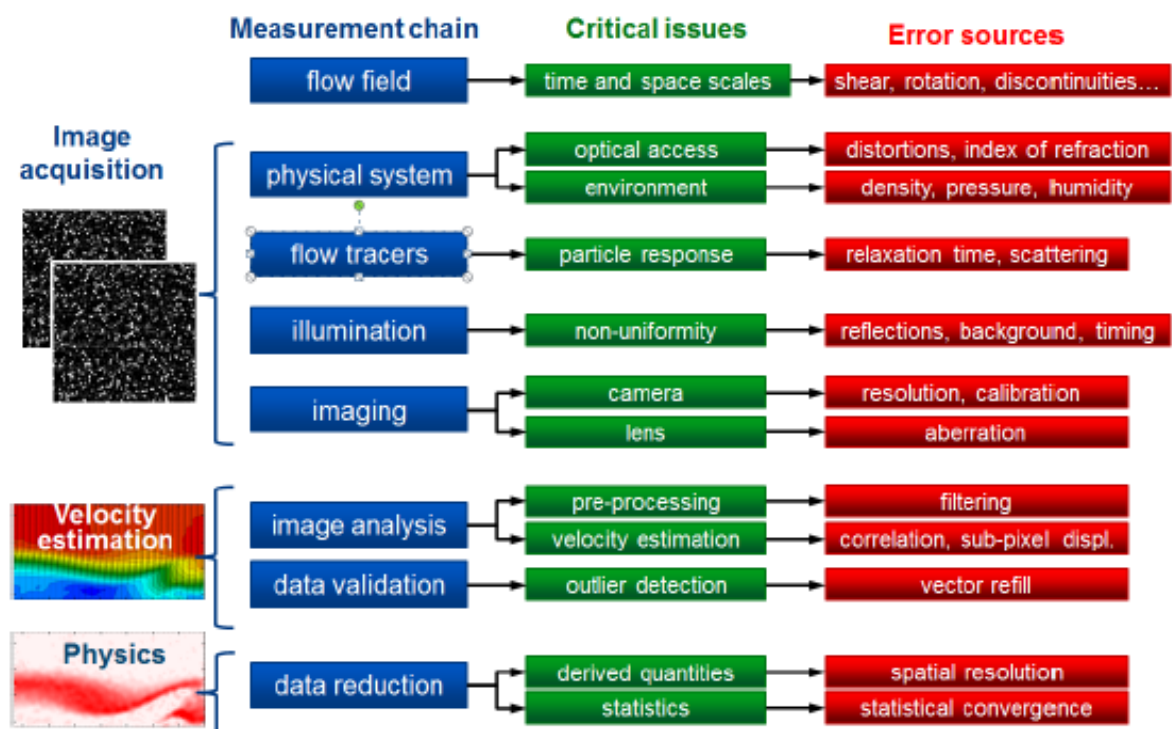


Figure 34 Overview of PIV error sources [23]

This is main reason for focussing on the quantification of the random error components in all of the method. Following are the main contributors in the uncertainties of the PIV methods.

- Timing and synchronization errors
- 2D-PIV perspective errors
- Particle response and lag
- Stereo-PIV:
  - Light sheet misalignment.
  - Inaccurate calibration targets.
  - Insufficient calibration model.



O Errors due to right/left camera viewing different interrogation volumes.[25]

### 2.11.1 TIMING AND SYNCHRONIZATION ERRORS

This error is introduced when there is time delay between the triggering of the laser and the actual light output. In case of the double pulsed laser source this lag can be avoided by continuously measuring the light output time by using the photodiode for both the emitted pulses. Then by delaying the trigger pulse time for one of the laser.

The timing error can also be introduced because of the switching time between the camera first and second exposure. There is shortest delay between the exposure switching and this delay is varied from camera to camera. This delay can be the limiting factor for the shortest laser pulse time.[23]

### 2.11.2 STEREO-PIV ERRORS

As we know the tolerances in the calibration plate can lead to deviation in the magnification scale or can induced the error in the co-ordinate system. The remedial solution for this error is to use the high quality plate. Also other method to tackle this problem to actually measure the marker position and feeding this correction in the calibration process.

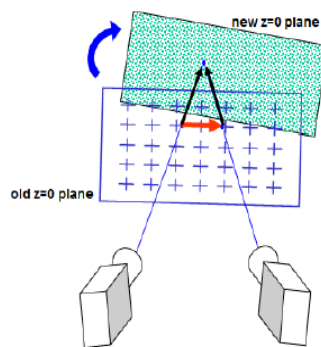


**Figure 35** Stereo PIV self-calibration procedure correcting misalignment of laser sheet [23]

There is also one most obvious error in the stereo PIV which is induced in the measurement as result of the cameras that are not having the same interrogation thickness because of the finite thickness of the light sheet. This substantial systematic error in the measurement can be because of any out of plane gradient. This systematic error also remains unnoticed in the



recorded images. The remedy for this will be use of the light sheet of the reduced thickness when out of plane velocity component is small enough.[23]

## 2.12 MEASUREMENT OF PRESSURE DISTRIBUTION FROM PIV EXPERIMENTS

In case of many engineering application velocity and pressure both are the important characteristic of the fluid flow and it is very much important to know the value of them for particular fluid. The phenomenons like cavitation, generation of drag and lift forces are completely dependent on the pressure variation over the flow field. As the velocity over a fluid field can be easily obtained but the pressure is still a problem. There have been some methods which give the pressure variation but it cannot be used simultaneously with PIV.[26]

For solution of this problem was found out by taking the help of the momentum equation. In momentum equation if the values of velocity components are inserted in the momentum equation and direct spatial integration over the flow domain is performed. As the spatial integration is easy to perform the care must be taken while selecting the path of the integration. Because there is possibility of the change in the pressure solution as there is change in the path of the integration.[27]

The pressure also can be found in case of the incompressible flow in this case the pressure distribution can be obtained by solving the pressure Poisson equation. Using the divergence operator on the incompressible Navier stoke equation a pressure Poisson equation can be derived. In case of the two dimensional, steady an incompressible flow the pressure field can be estimated through the numerical integration of the steady Navier- stokes equation.

$$U \frac{\partial U}{\partial X} + V \frac{\partial U}{\partial Y} = -\frac{\partial p}{\partial X} + \nu \left( \frac{\partial^2 U}{\partial X^2} + \frac{\partial^2 U}{\partial Y^2} \right) \quad (2.26)$$

$$U \frac{\partial V}{\partial X} + V \frac{\partial V}{\partial Y} = -\frac{\partial p}{\partial Y} + \nu \left( \frac{\partial^2 V}{\partial X^2} + \frac{\partial^2 V}{\partial Y^2} \right) \quad (2.27)$$

By using finite difference approximation of the velocity gradients  $\partial p/\partial X$  and  $\partial p/\partial Y$  are obtained. After this the pressure gradients are integrated for which the limit starts from the point near to the centre having initial value of  $p_o$ .

Another approach for pressure field estimation from incompressible PIV velocity data is using the integration of the Poisons pressure equation.



$$\nabla^2 p = -\rho \nabla \cdot (U \cdot \nabla U) \quad (2.28)$$

For pressure on surfaces, Neumann boundary condition can be easily obtained from Navier-Stokes equation.

$$-\nabla p = \rho \frac{\partial U}{\partial t} + \rho \cdot (U \cdot \nabla) U - \mu \nabla^2 U \quad (2.29)$$

Considering the case of the flow around the object, the flow is steady in the far field, outer boundary condition can be represented by using the Dirichlet condition  $p=0$  this equation provides the integration of equation across the field of view. In this approach the term  $dU/dt$  in equation is considered to be zero. This can be one of the limitations for using this technique.

Another approach which introduces the control volume method to get the variation in pressure fields across the fluid flow. This method has an advantage over above method as time resolved data allows the proper treatment to acceleration term.

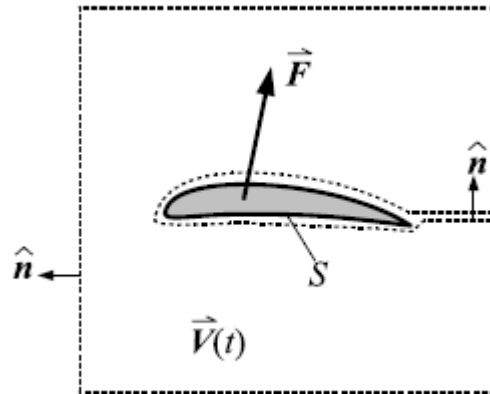


**Figure 36** Control-Volume approach for determining integral forces from two dimensional flow [27]

In one of the previous researches the estimation of the pressure gradient was based on the potential flow theory in the inviscid region. whereas the Navier stokes equations were integrated between two points belonging to the viscous region. The time- means pressure can be obtained from

$$-\frac{\partial \bar{p}}{\partial x_i} = \rho \bar{u}_j \frac{\partial \bar{u}'_i}{\partial x_j} + \rho \frac{\partial \bar{u}_i \bar{u}_j}{\partial x_j} - \mu \frac{\partial^2 \bar{u}_i}{\partial x_j \partial x_j} \quad (2.30)$$



It is clearly evident from the equation all terms from the right hand side of the equation can be derived from statistically averaged PIV data. Approximate integration can further help to estimate the time –mean pressure and body forces.[3]



### 3 EXPERIMENTAL SETUP AND MEASUREMENTS

The PIV experimental setup was designed in the PIV lab of the university. Following picture shows the experimental arrangement done during the measurement of the stereo PIV and 3D Tomo-PIV.

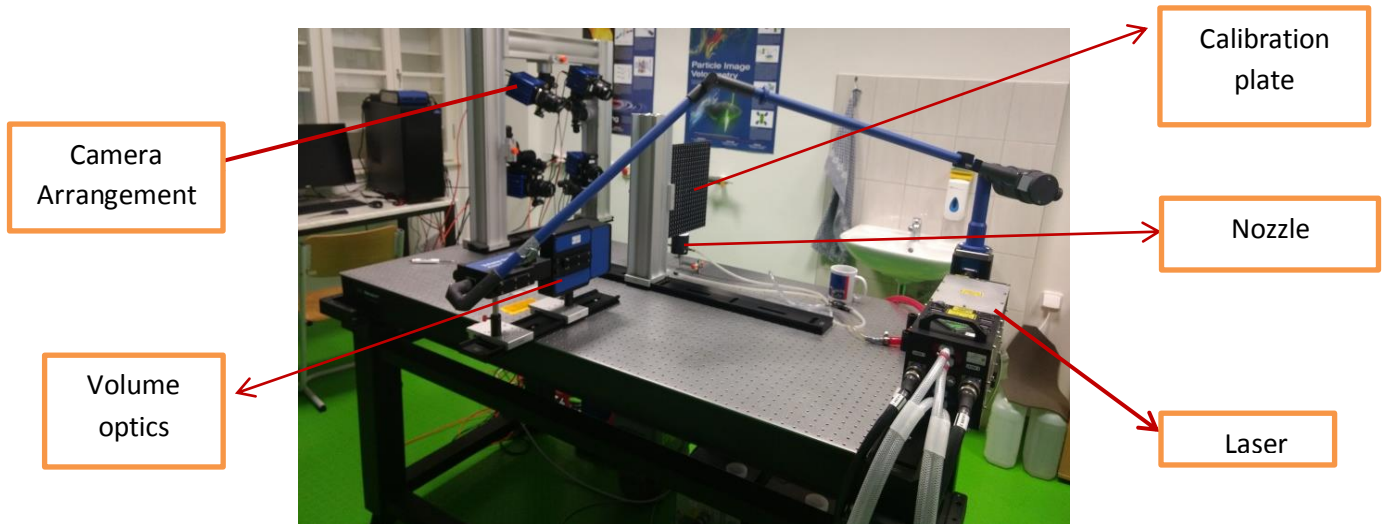


Figure 37 Experimental Setup

#### 3.1 COMPONENTS AND THERE SPECIFICATIONS

##### 1. Camera

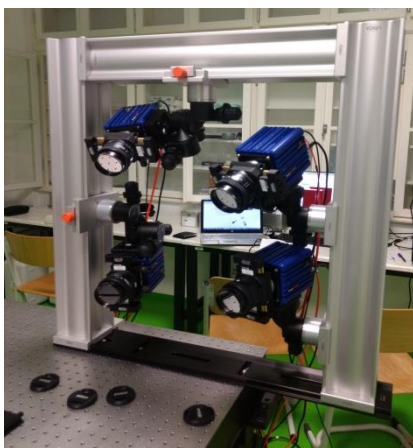


Figure 38 Orientation of the camera\*

##### Camera specification

*sCMOS* : This combines best of CCD and CMOS.

- Readout noise :  $2 e^-$  rms
- Imaging frequency : 50fps@full frame
- Dynamic range : 16 bit
- Resolution : 2560 X 2160 Pixel

*\*The cameras orientation was same during the stereo measurement and 3D Tomo-PIV measurement. In case of the stereo PIV recording top two of the cameras were inoperative.*



## 2. Scheimpflug adapter

The Scheimpflug adapter has been used in the experimental setup. The adapter serves the purpose of the tilt and as well as rotation purpose

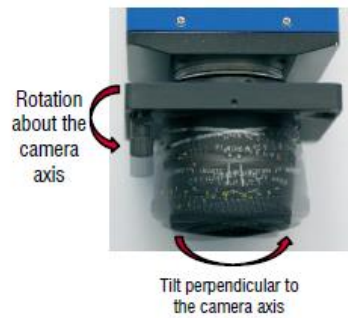


**Figure 39** *Scheimpflug adapter*

## 3. Nozzle

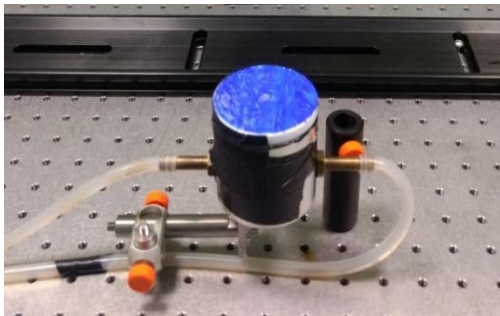


**Figure 40** *Nozzle*

### Nozzle Specification

The nozzle diameter is 8mm and particles are accelerated with the help of compressor.

## 4. Particle generator (Aerosol)

The particle generator has been used in conjunction with the compressor to get the required push for the particles and to achieve the intended velocity.

- Max working Pressure : 6 bar
- Working liquid : Vegetable oil



**Figure 41** *Particle generator*

## 5. Dual Pulsed Laser



**Figure 42** *Dual Pulsed laser*

### Specification: Evergreen

- Flash lamp –pumped Nd : YAG
- Wavelength 532 nm
- Pockets cell
- Max. Pulse energy typ. 100-200mJ  
Max.frequency range typ. 15Hz (Up to 100Hz)



The working of dual-pulsed Nd : YAG laser has been explained in the above section (page no 10). The laser used during the experiment has been used along with the Q-switch and flash lamp. The brief working principle of the q-switch and flash lamp is explained below.

## Q-SWITCH PRINCIPLE

Q-switch helps to use the laser in the triggered mode. The principle of working of the Q switch is shown in the figure below.

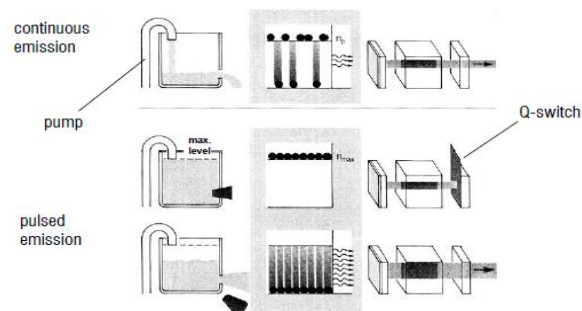


**Figure 43** *Q-switch Principle* [8]

## FLASH LAMP TO Q-SWITCH PRINCIPLE

As during the measurements flash lamp and Q-switch work in sync for proper performance of the laser. Their combined working principle can be seen in figure below.

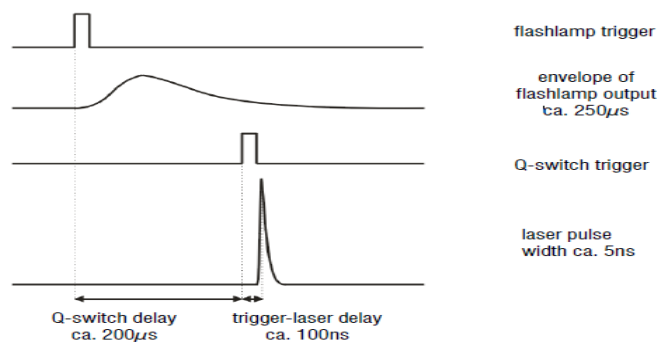


**Figure 44** *Flash lamp to Q-switch principle* [8]





## 3.2 MEASUREMENTS

For both of the measurements the calibration is carried out using the calibration plate. The triangulation method as discussed in previous part was used to carry out the calibration process. In simple words calibration is said to be carried out to identify the particle seen by different cameras as single particle. During the measurement 100 images were recorded for each condition.

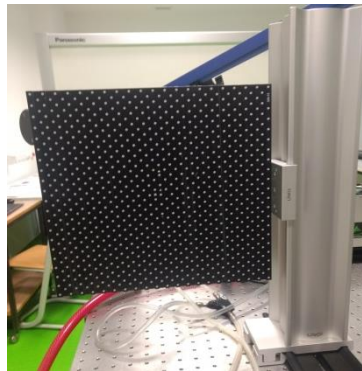


**Figure 45** Calibration plate

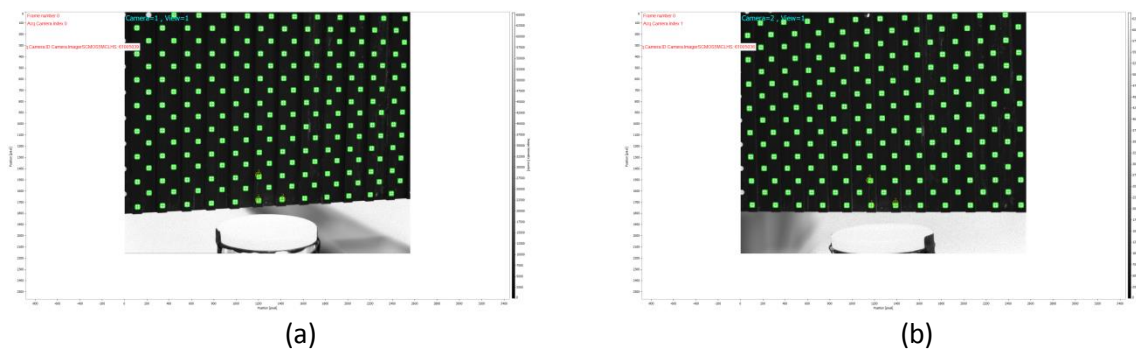


**Figure 46** Calibration plate image from the system after calibration (StereoPIV)

**Some parameters which were maintain constant during the measurement :**

Recording type : Time based recording	Camera 1 Image transformation : None
Image rate : 2 Hz	Camera 2 Image transformation : 180°
Trigger rate : 15 HZ	Camera 3 Image transformation : 90°
Trigger source : Internal	Camera 4 Image transformation : None

**Table 3** Other important parameters for measurement



### 3.2.1 STEREO PIV

The interrogation window size for the measurement was (64 x 64) pixel and the overlay was 75%. The measurement of the Stereo PIV was carried on varying two parameters:

#### 1) Laser Power:

Laser power has been selected on the basis of the previous researches suggested range for stereo-PIV and Tomo-PIV (3%-10%)

#### 2) Laser Pulse time:

Laser pulse time has been selected on the trial and error method. The trial started with the 10  $\mu$ s, Around 30  $\mu$ s required intensity was achieved.

Sr No.	Laser Pulse Time ( $\mu$ s)	Laser Power (%)
1	30	3
2	30	5
3	40	3
4	40	5

**Table 4** Stereo-PIV measurement

### 3.2.2 TOMO-PIV

Similarly the measurements for the Tomo-PIV were taken on the same parameter but the laser power was on the higher side such that it can illuminate all the volume.

Sr No.	Laser Pulse Time ( $\mu$ s)	Laser Power (%)
1	30	30
2	40	30

**Table 5** Tomo-PIV measurement



## 4 RESULTS AND DISCUSSION

### 4.1 STEREO PIV

The measurements for stereo PIV were taken with nozzle exit velocity ( $V_o$ ) is 5.67 m/s and corresponding Reynolds no is 3070. All images were taken at the centreline plane of the jet, where the origin is located on the centreline of the nozzle exit. Axial direction of the stream is represented by the Y-axis; similar. The quantities  $V$ ,  $U$ ,  $W$  represents components of the velocity along Y,X,Z-axis respectively.

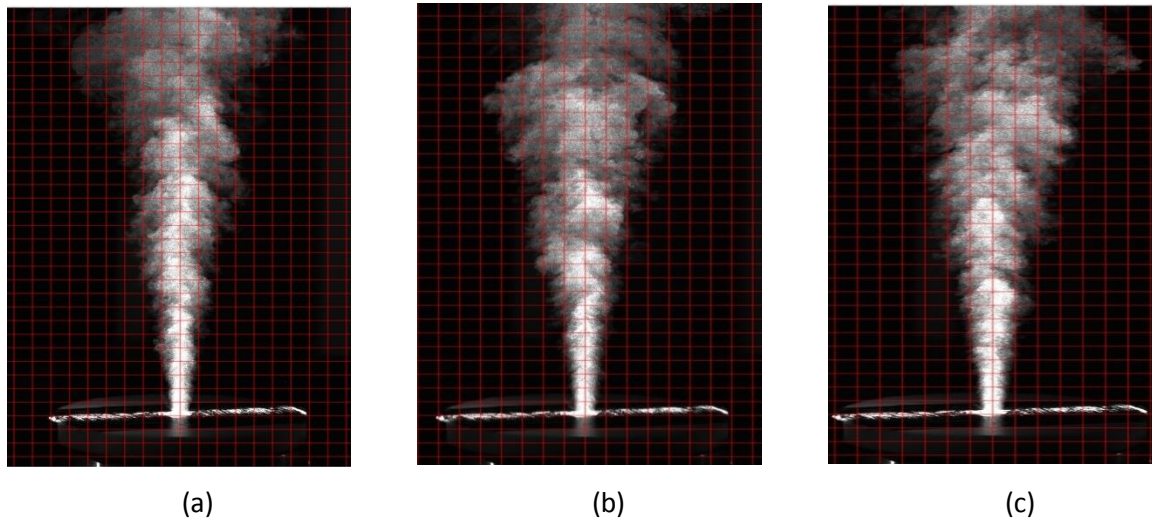
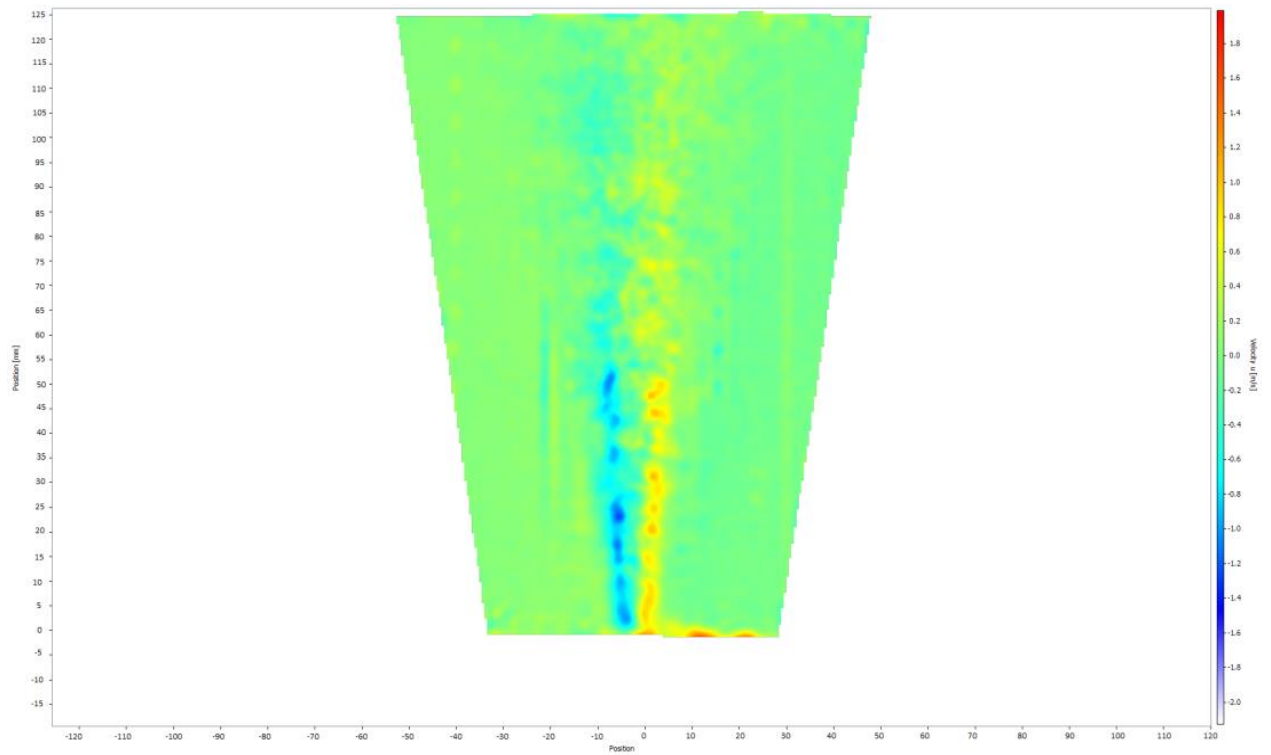


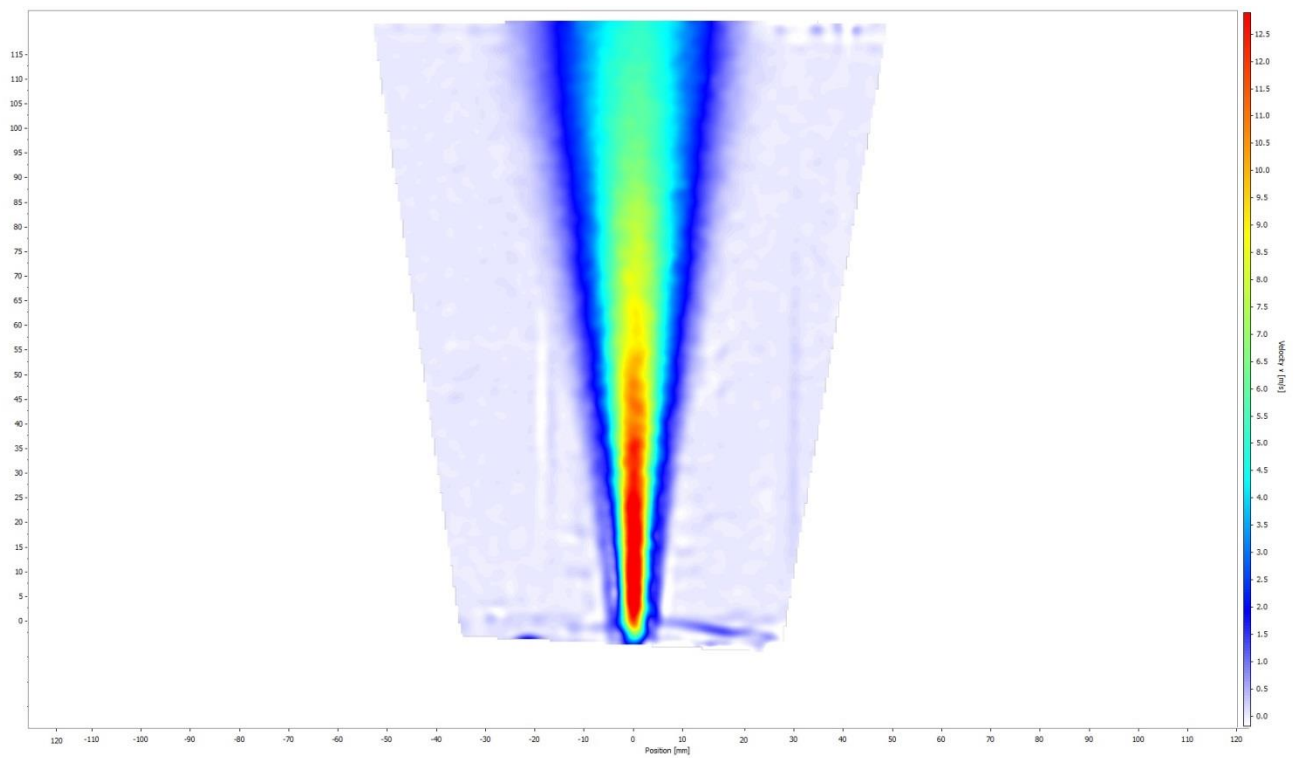
**Figure 47** Structural development of the free jet along the axial direction of the stream.

From the figures shown above zones which are discussed in the section 1.1 can be clearly seen in all the three figures. By observing particles in the transition zone in fig (a) as they further reach the self-similar zone some of the particles can be clearly seen of generating vortices along the shear layer fig (b). In fig (c) the particles enter in the termination region.



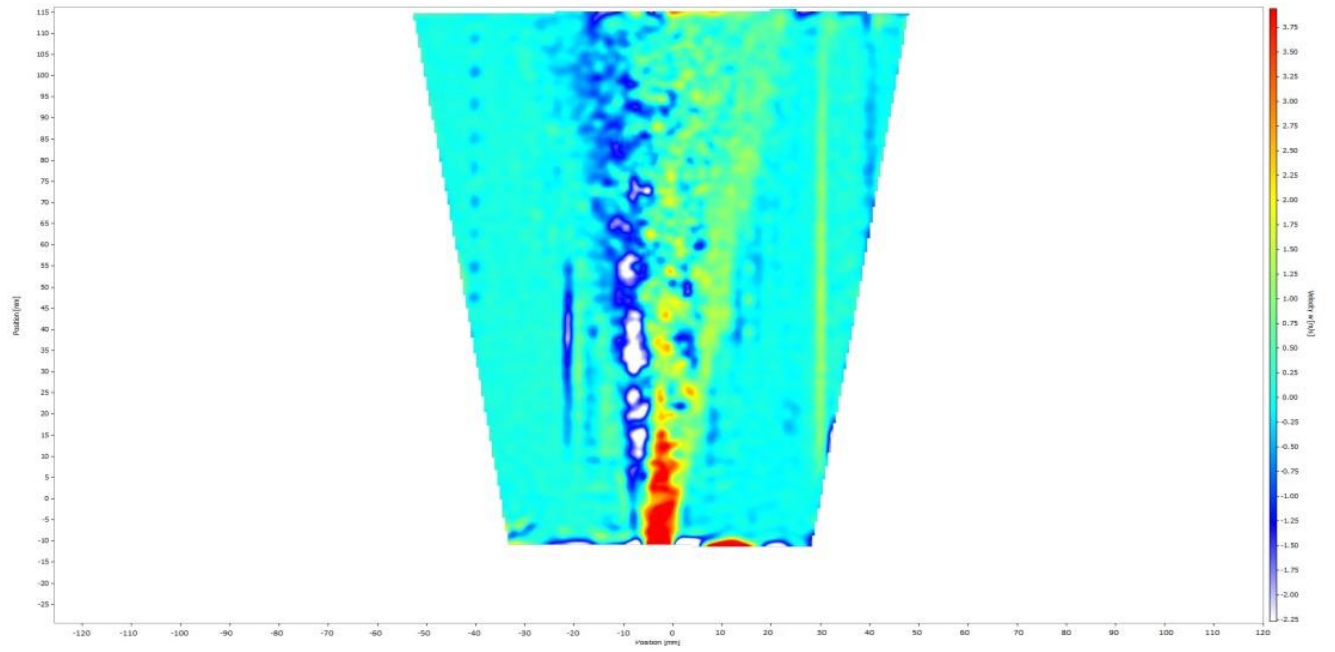


*a) U-component of the velocity*

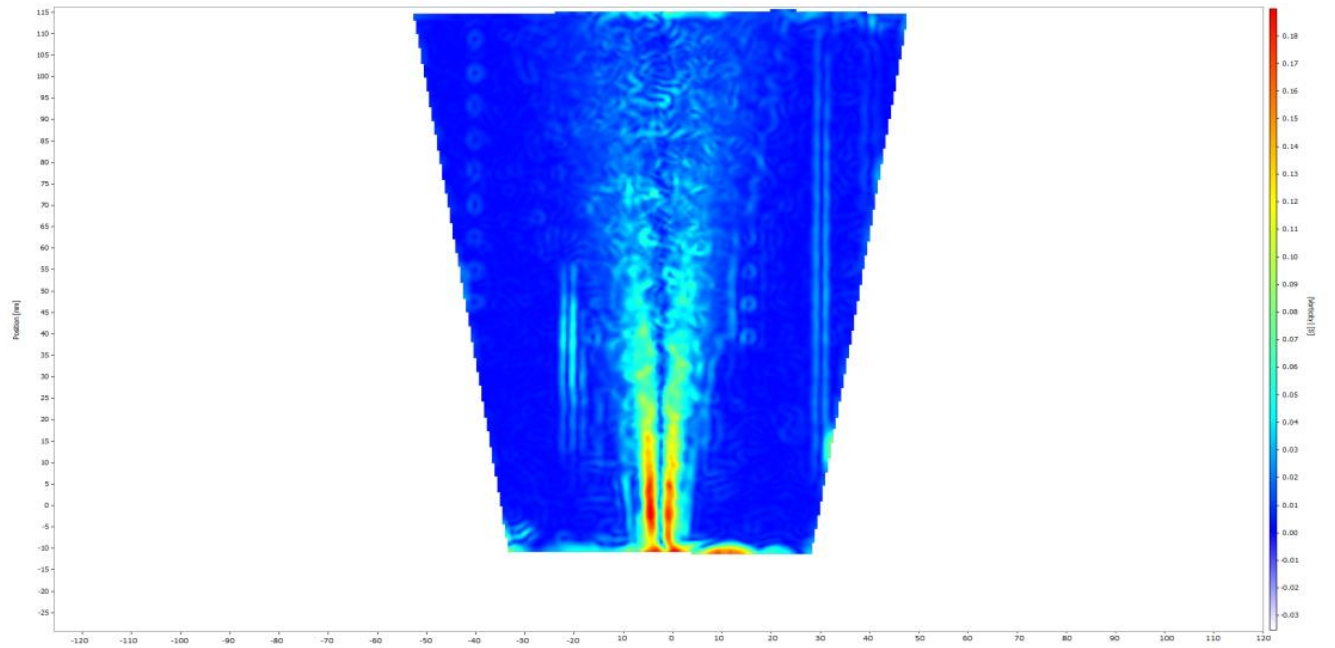


*b) V- component of the velocity*



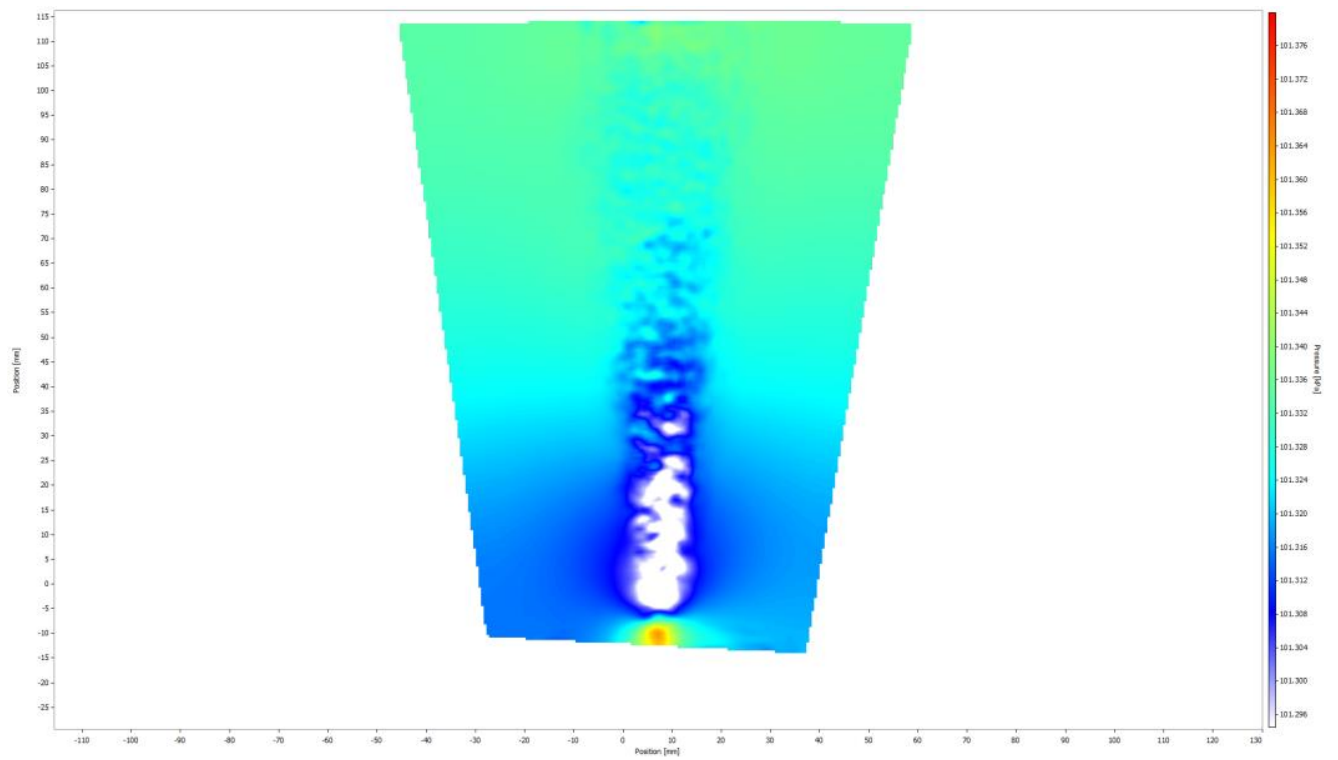


*c) W-component of the velocity*



*d) Vorticity along flow field*





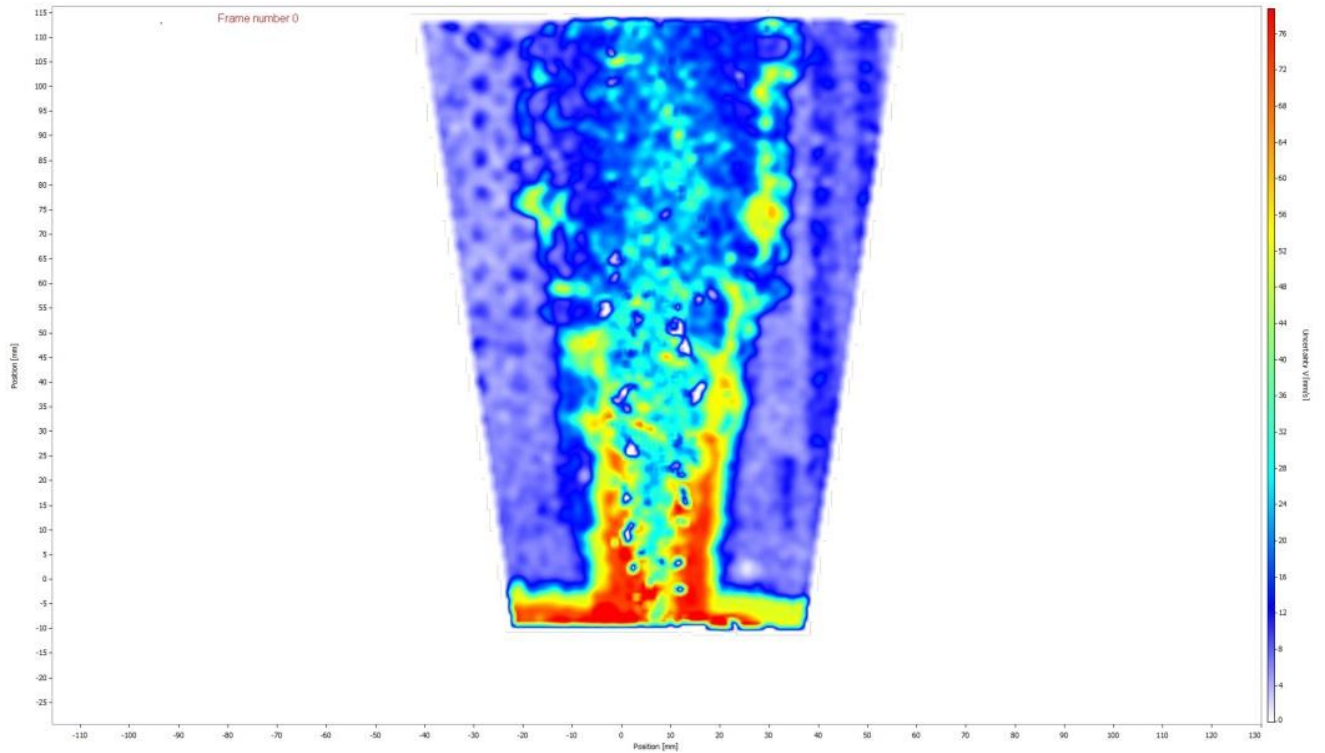
*e) Time averaged pressure*



*f) Raw image of the jet*







g) Uncertainty in velocity

**Figure 48** Flow characteristics of the stereo PIV measurement with  $30\mu\text{s}$  laser pulse time and 3% laser power

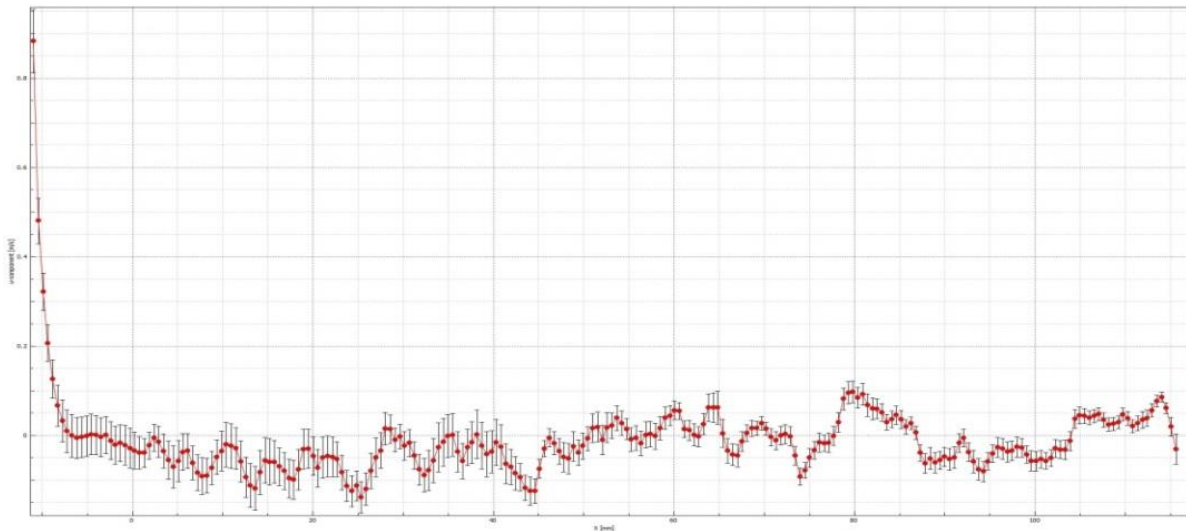
The fig (a) shows the u-velocity component of the flow over entire field .As we know from the previous research boundary layer acts as the free shear layer at the nozzle exit. The figure also describes shear layer development on the either side of the stream flow. The fig (b) represents the actual flow velocity across its axis. As we know from the law of conservation of momentum the velocity of the jet increases as it leaves the nozzle this value goes on increasing until it reaches its peak value. Further the downward trend in the velocity can be clearly seen in the figure (b). During the measurement the maximum peak value obtained is  $4.40 V_0$  this value was found in the core of the jet stream.

As the vorticity displayed in the Fig (d) displays the rotational movement of all the particles all over the flow field. As the ambient fluid start to entrain into the main stream fluid the vortices formation rate increases this is clearly evident from the fig (d). The increased vortices can be clearly seen at some distance from the nozzle and the vortices i.e. the value of the rotational component is higher in the self-similar zone. The reason for this is as we go far from the nozzle the ambient fluid entrainment increases so as the vorticity. The value of the vorticity the field was found to be 0.08 rotations per second in the self-similar zone.



As per the continuity equation the jet velocity goes on increasing on the other hand the pressure values goes on decreasing after the nozzle exit. As per discussion in theoretical section above the time averaged pressure value has been calculated from the available velocity data. The decrease in the pressure value can be clearly seen in the fig (e). The pressure drop across the nozzle was less than the 1 kPa. The raw image of the jet can be seen in the fig (f).

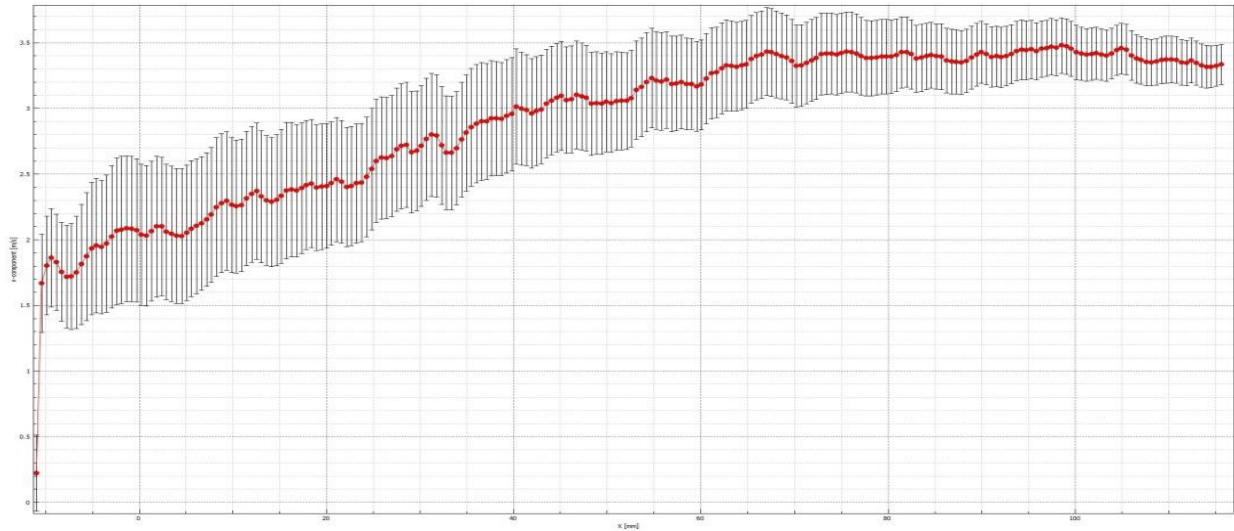
The graph of the velocity vs. the particle position from the nozzle has been plotted along with the uncertainties present in the velocity. In this the uncertainties were represented around each point location in the graph. The graph has been plotted for all three components of the velocities with the help of the PIV software.



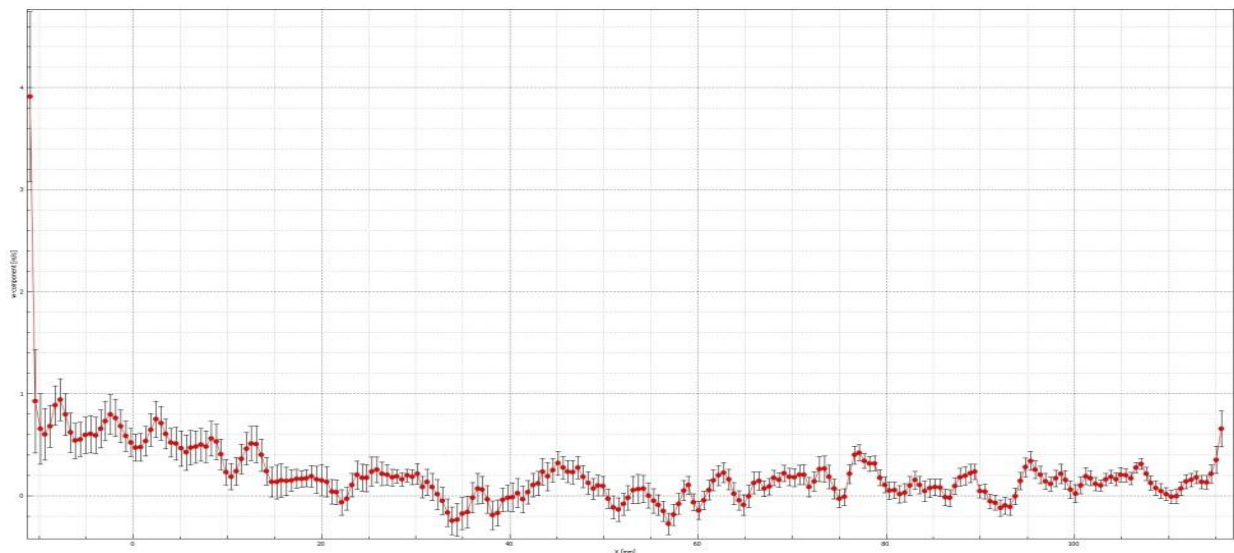
*(a )U-component of velocity*







(b) V- Component of velocity



(c) W-Component of velocity

**Graph 1** Graphical representation of the a) U-component of the velocity b) V-Component of the velocity  
c) W- Component of the velocity

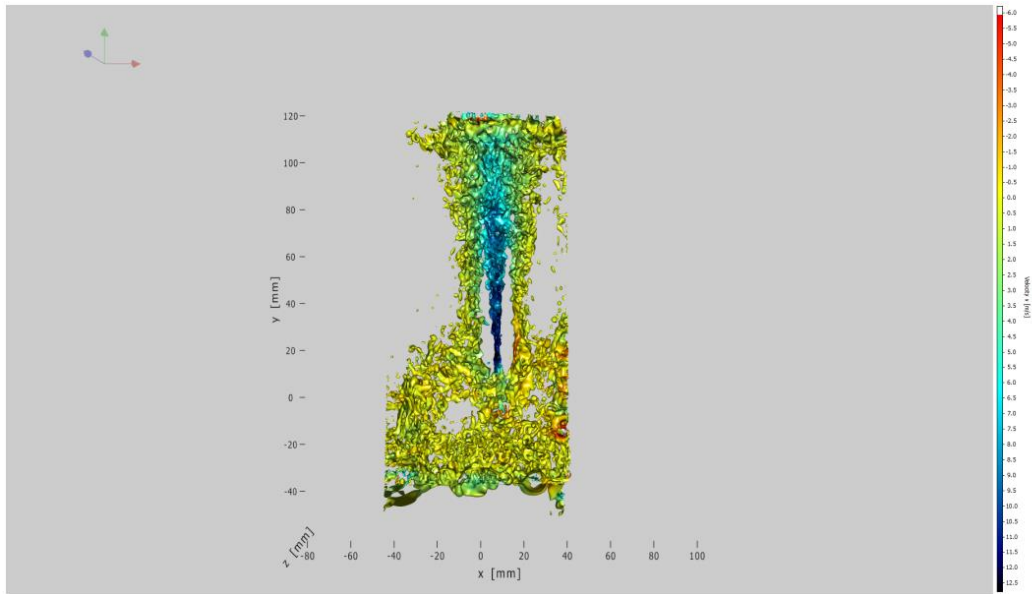
## 4.2 TOMO-PIV

The Tomo-PIV has followed some different post processing technique. In this the recording images were pre-processed. Basically in the pre-processing the images were applied with geometrical mask. This mask helps us to focus on the area of interest and also helps to reduce the unnecessary computation time.

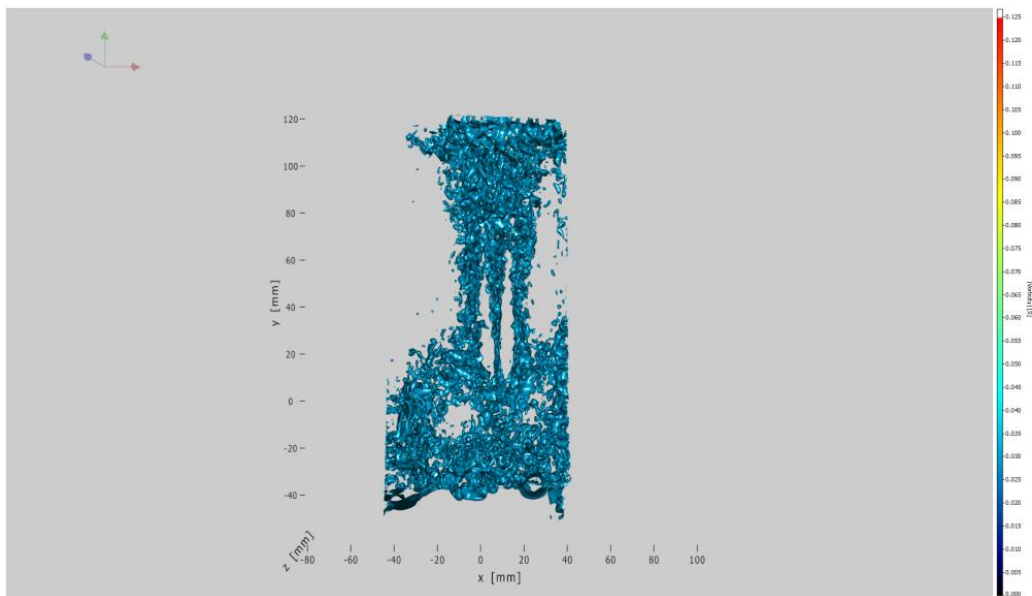
The result pattern for the stereo-PIV and Tomo-PIV has been quite similar for all the flow characteristics like vorticity development; pressure drop across the nozzle exit. All Flow



characteristics of the Tomo PIV measurement are for  $40\mu\text{s}$  laser pulse time and 30% laser power.



(a)

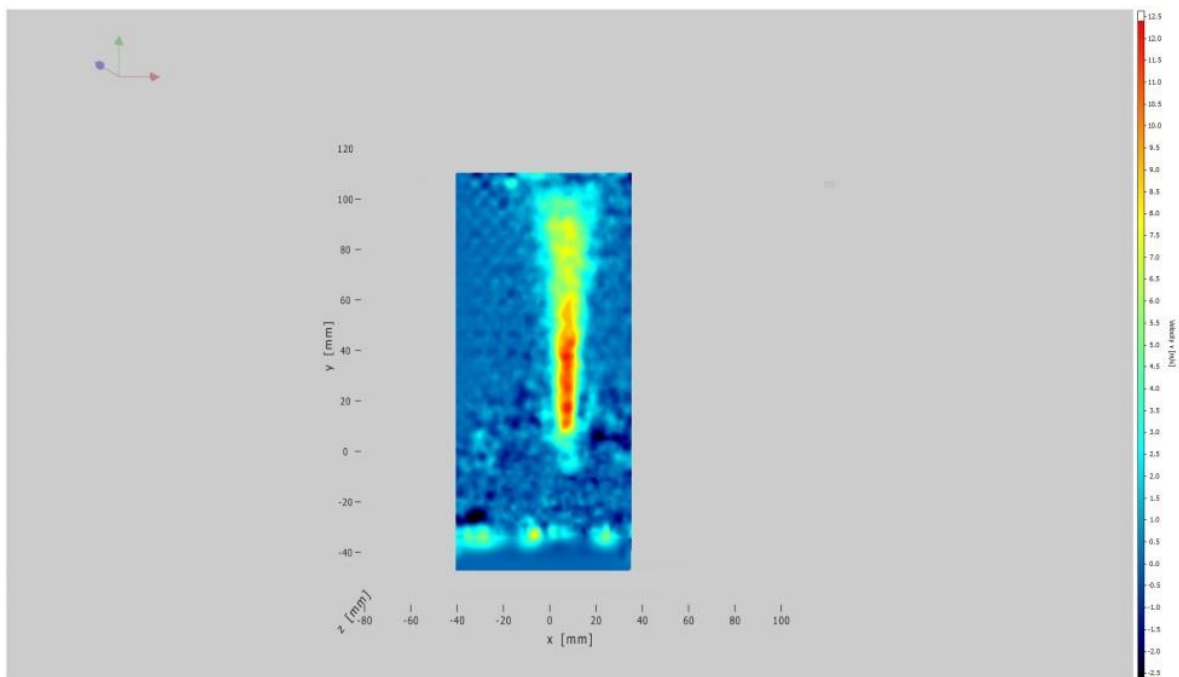


(b)

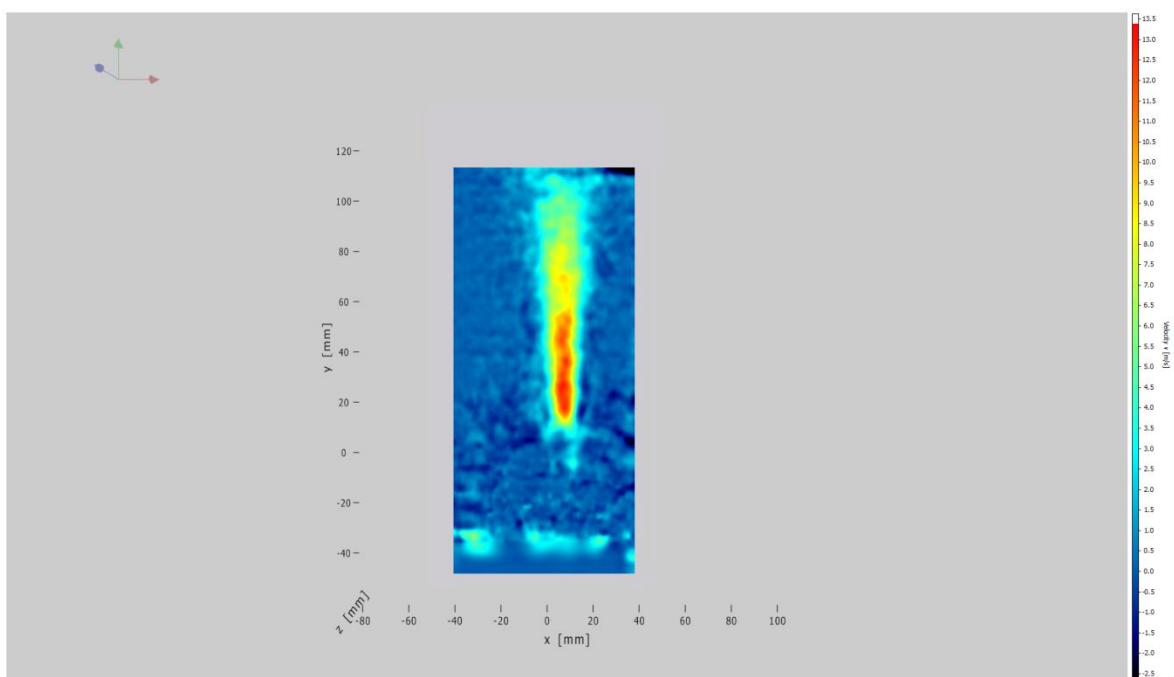
**Figure 49** Iso-surface generated at the nozzle exit a) axial velocity component b) Vorticity

For measurement the z-direction dimension is 10mm, in which the nozzle is located at the centre.



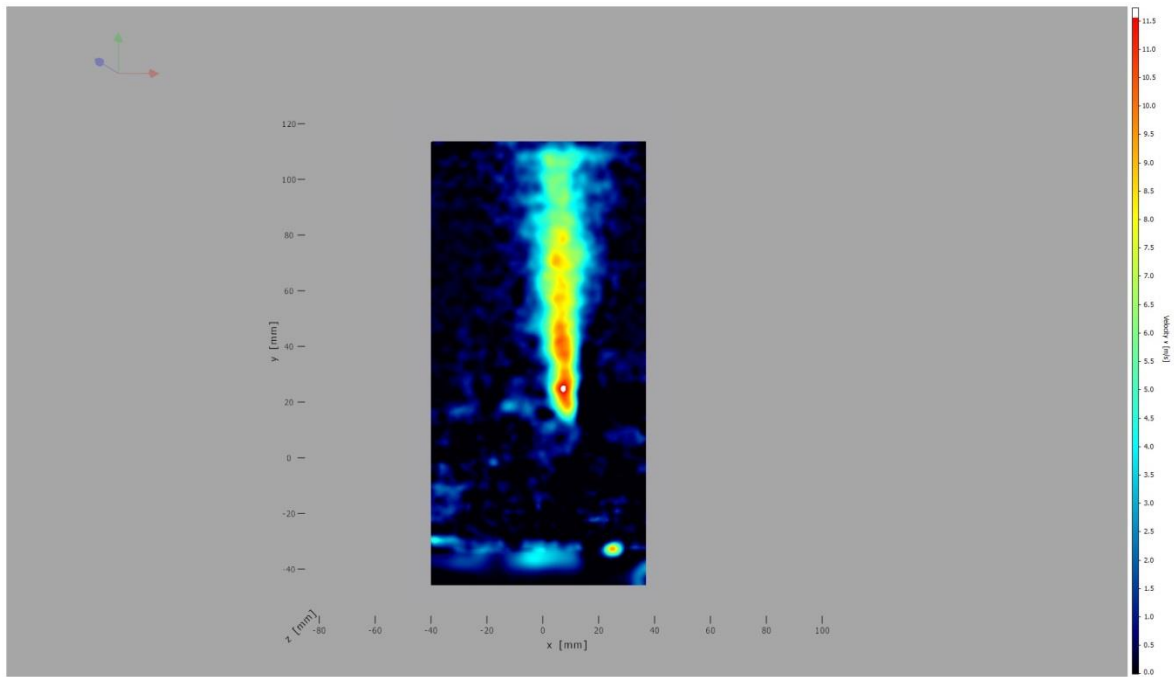


(a)



(b)

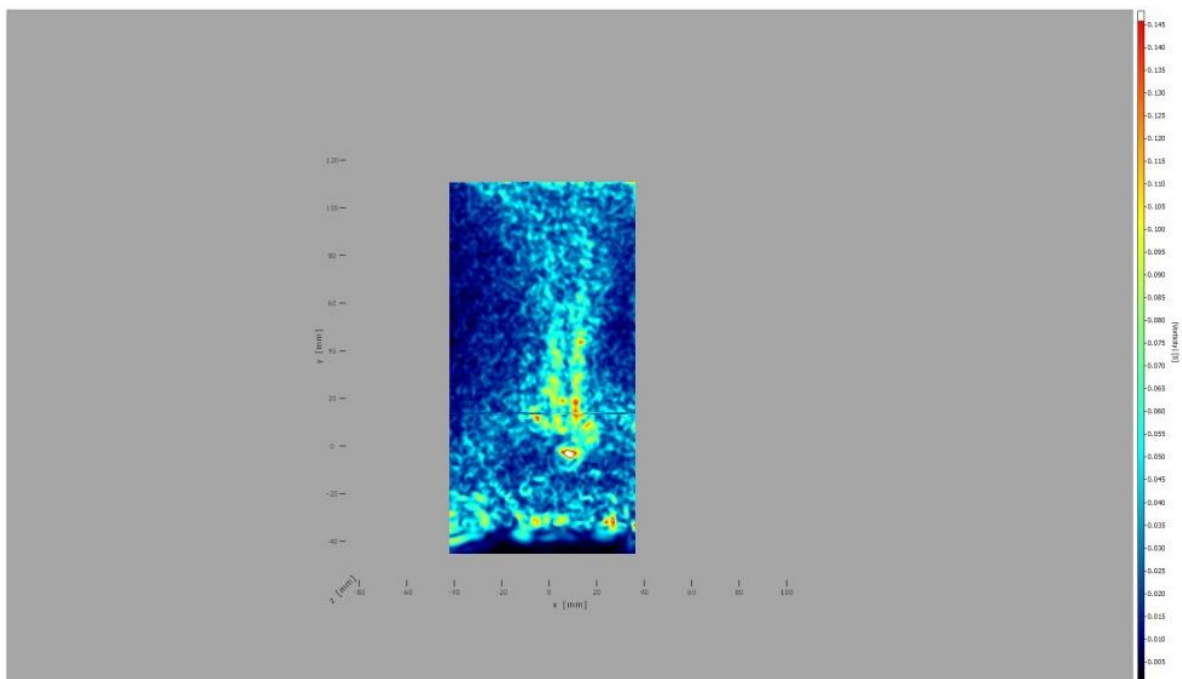




(c)

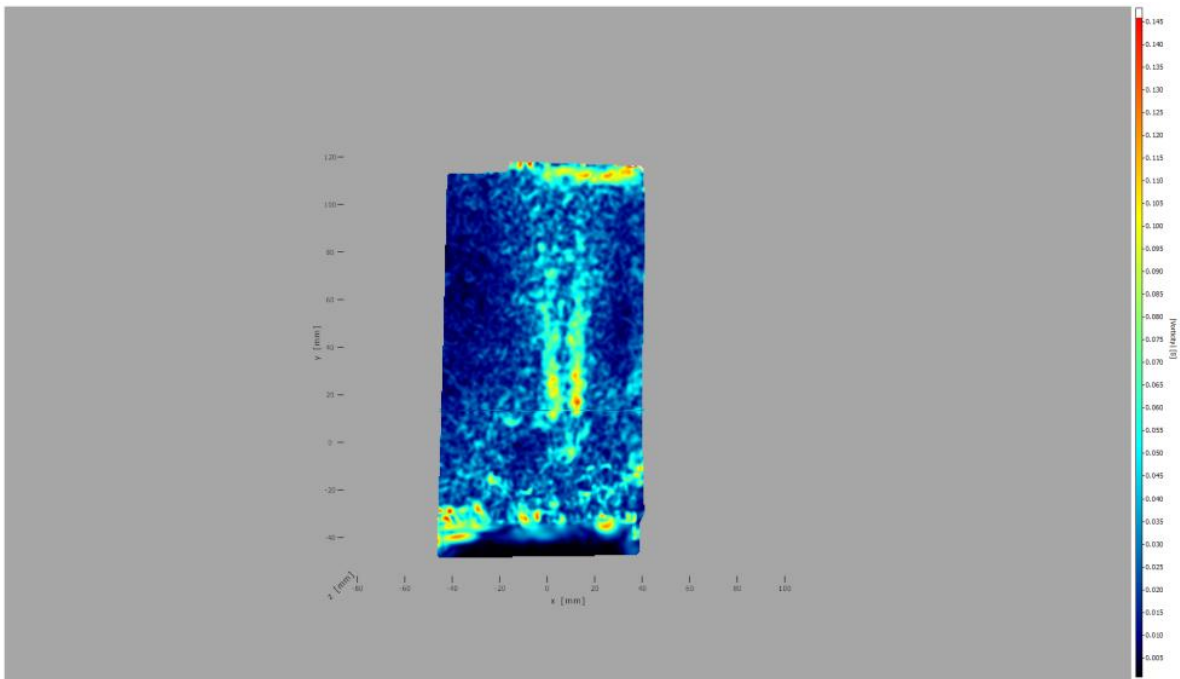
**Figure 50** Vector slices of the velocity for the axial component of the velocity (a) at  $z=-5$  (b)  $z=0$  (c)  $z=5$

Similarly the vector slices for different values of  $z$  were studied for understanding the vorticity pattern in the experimental volume.

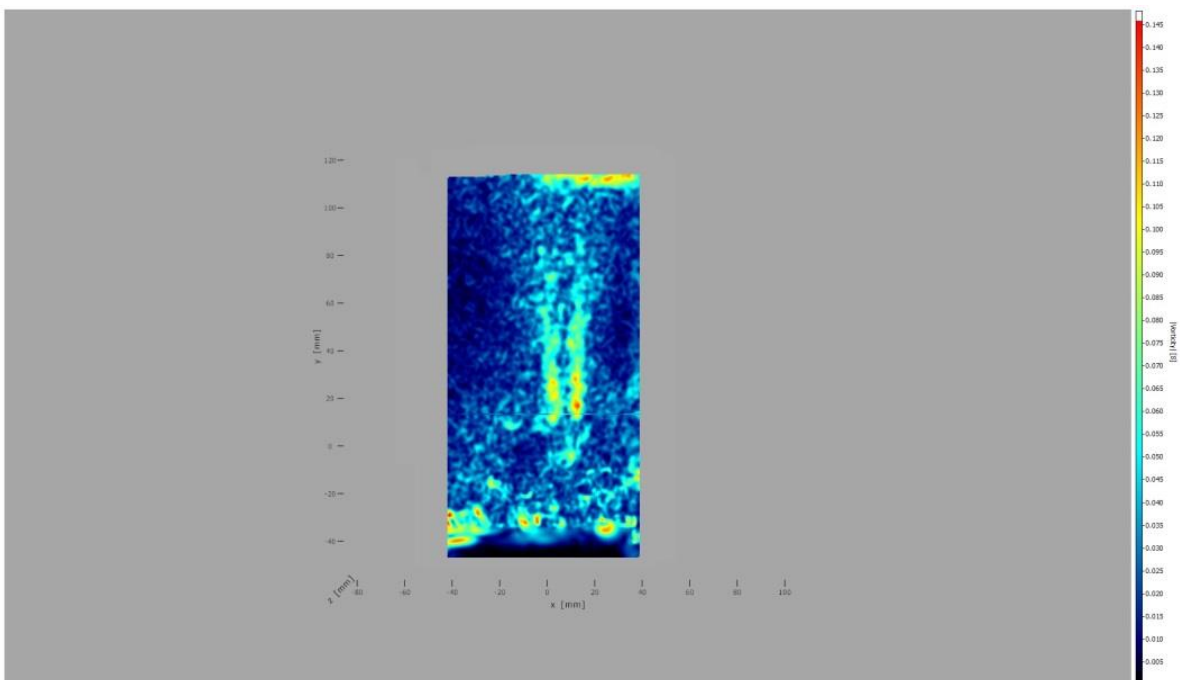


(a)





(b)



(c)

**Figure 51** The vorticity behaviour at a)  $Z=-5$  b)  $Z=0$  c)  $Z=5$



Average pressures were calculated from the obtained velocity data as discussed in the previous sections.

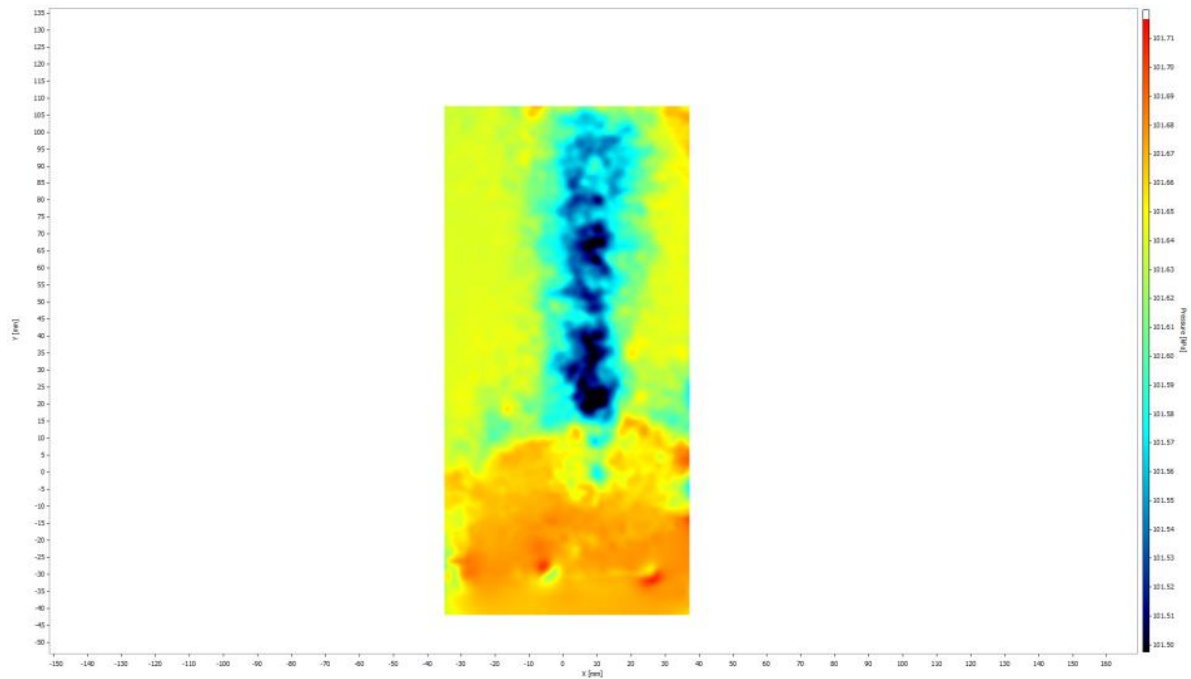
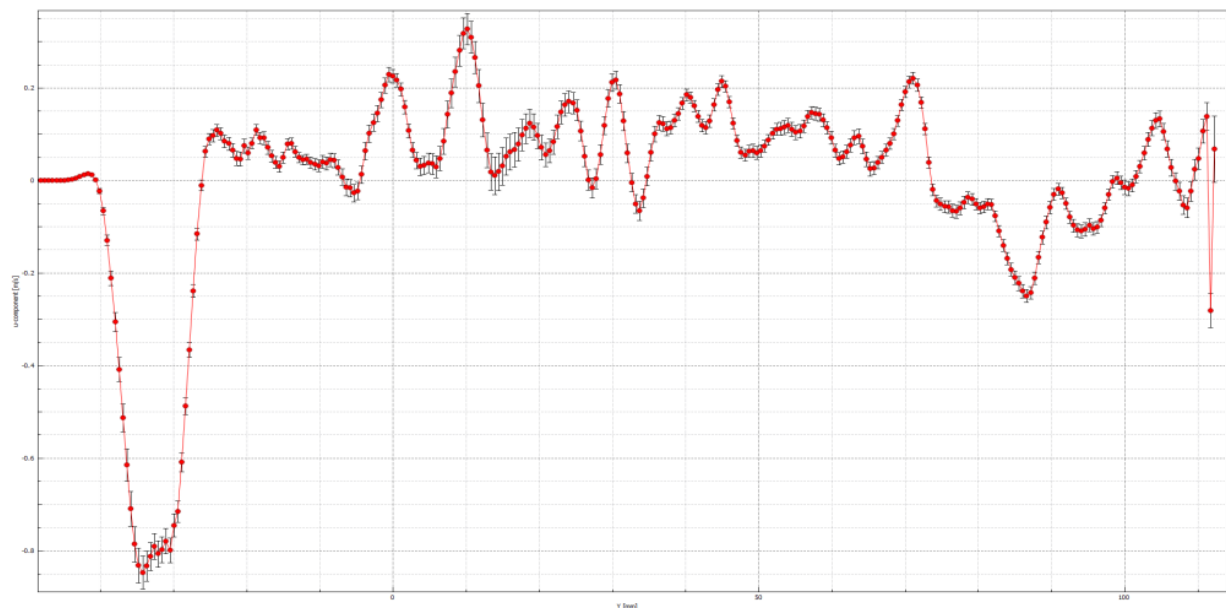


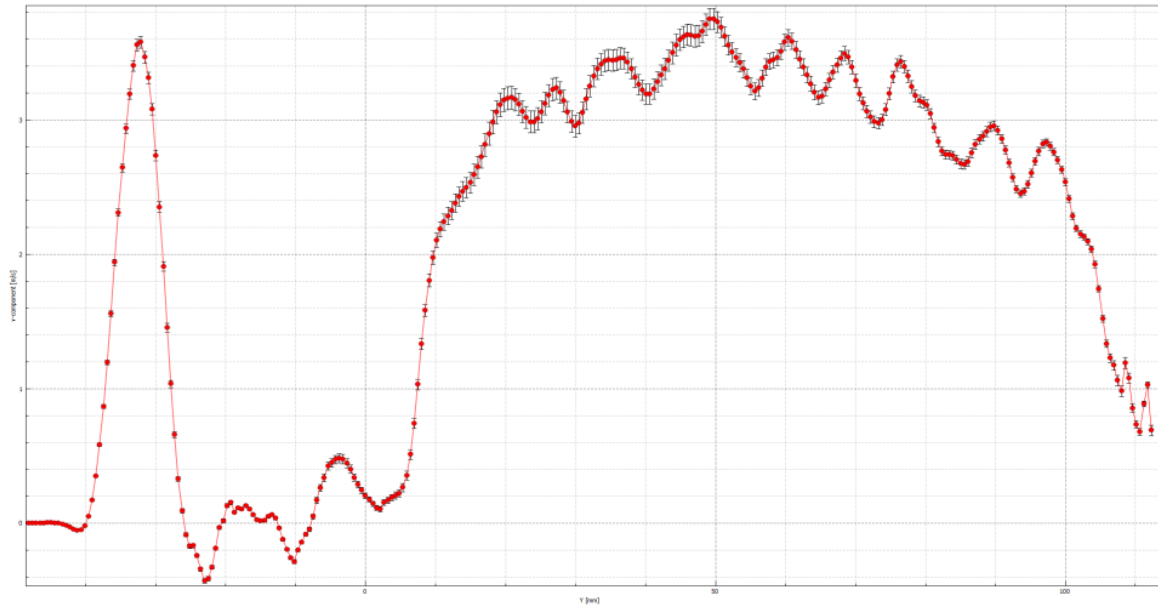
**Figure 52** Time averaged pressure over the flow field

The graph of the velocity vs. the particle position from the nozzle has been plotted along with the uncertainties present in the velocity. The graph has been plotted for all three components of the velocities.

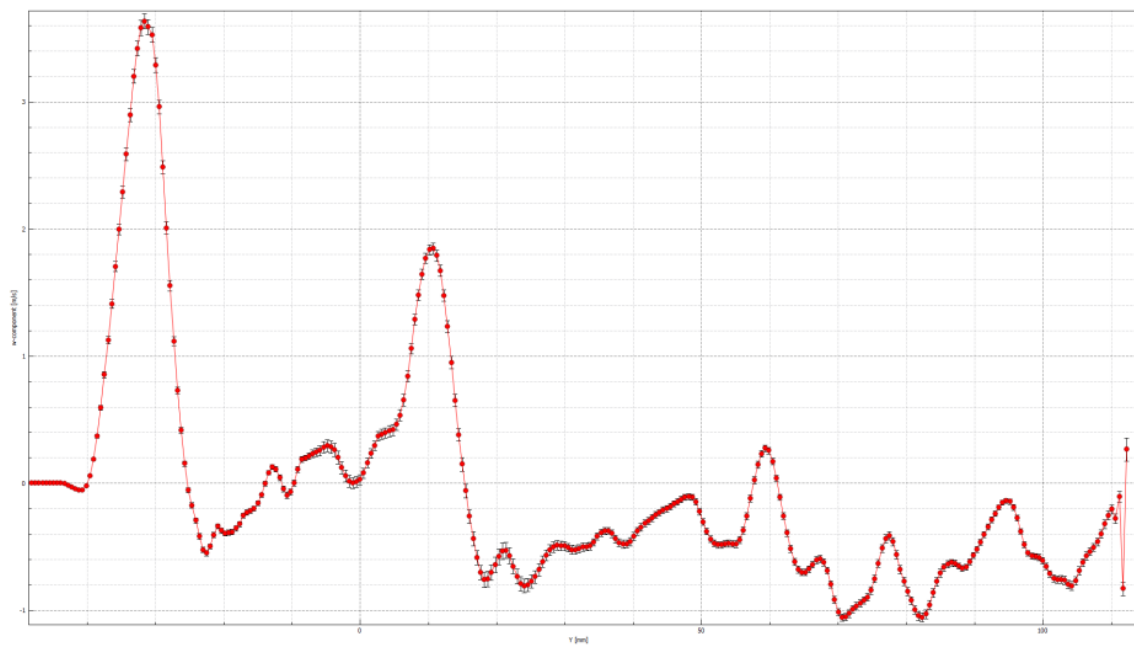


*(a) U-Component of velocity*





(b) V-Component of velocity



(c) W-Component of velocity

**Graph 2** Graphical representation of the a) U-component of the velocity b) V-Component of the velocity c) W- Component of the velocity



## 5 CONCLUSION

Stereo particle image Velocimetry and Tomo particle image Velocimetry was employed successfully. The study helped in understanding the structures and development of flow through the round jet. It also provided measurement of all three instantaneous velocity components in the centreline plane of a round air jet. With flow having Reynolds number 3070 the measurements were taken in the near field of the jet. The characteristics like vorticity, Time averaged pressure were measured and agreed with previous available literature.

The jet velocity ( $V_o$ ) at the nozzle exit found to be 5.67 m/s and highest velocity measures was  $4.40V_o$ . Highest velocity was found at distance from the nozzle exit. Also the pressure drop after the nozzle exit was less than 1kPa.

During the study of the vortices the small-scale vortex cores in the near field evolve and pair up with the vortices upstream to form larger-scale structures downstream as observed in the images and the velocity fields. This characteristic has been seen in the stereo PIV and Tomo-PIV as well.

### 5.1 FUTURE WORK

The currently the study was carried out for the flow characteristics generated by the round jet continuous nozzle. This work further can be extended to study the fluid flow characteristics generated by the synthetic jets. Also there is possibility of the work to be extended to try out the different geometrical shapes of the nozzle.





## REFERENCES

- [1] S. B. POPE, “An explanation of the turbulent round-jet/plane-jet anomaly,” *AIAA J.*, 1978.
- [2] C. G. Ball, H. Fellouah, and A. Pollard, “The flow field in turbulent round free jets,” *Progress in Aerospace Sciences*. 2012.
- [3] S. Ghaemi, D. Ragni, and F. Scarano, “PIV-based pressure fluctuations in the turbulent boundary layer,” *Exp. Fluids*, 2012.
- [4] A. A. Abdel-Rahman, S. F. Al-Fahed, and W. Chakroun, “The near-field characteristics of circular jets at low Reynolds numbers,” *Mech. Res. Commun.*, 1996.
- [5] B. Ganapathisubramani ‡, E. K. Longmire, and I. Marusic, “Investigation of three dimensionality in the near field of a round jet using stereo PIV,” *J. Turbul.*, vol. 3, no. October 2012, p. N16, 2002.
- [6] S. Green, “Fluid vortices,” *Int. J. Multiph. Flow*, 2002.
- [7] T. Matsuda and J. Sakakibara, “On the vortical structure in a round jet,” *Phys. Fluids*, 2005.
- [8] M. Raffel, C. E. Willert, S. T. Wereley, and J. Kompenhans, *Particle Image Velocimetry - A Practical Guide*. 1989.
- [9] J. Westerweel, G. E. Elsinga, and R. J. Adrian, “Particle Image Velocimetry for Complex and Turbulent Flows,” *Annu. Rev. Fluid Mech.*, 2011.
- [10] E. Huber and M. Frost, “Light scattering by small particles,” *Aqua*, 1998.
- [11] C. Willert, B. Stasicki, J. Klinner, and S. Moessner, “Pulsed operation of high-power light emitting diodes for imaging flow velocimetry,” *Meas. Sci. Technol.*, 2010.
- [12] A. Melling, “Tracer particles and seeding for particle image velocimetry,” *Meas. Sci. Technol.*, vol. 8, no. 12, pp. 1406–1416, 1997.
- [13] Echols, W.H. and J. A. Young, “Studies of portable air-operated aerosol generators,” *Nav. Res. Lab. Rep.*, 1963.
- [14] R. Lindken and W. Merzkirch, “A novel PIV technique for measurements in multi-phase flows and its application to two-phase bubbly flows,” in *DLR-Mitteilung*, 2001.
- [15] E. Hecht, “Optics 2nd edition,” *Addison-Wesley Publishing Company 1987*. 1987.
- [16] M. Raffel, C. E. Willert, J. Kompenhans, M. Raffel, C. E. Willert, and J. Kompenhans, “Image evaluation methods for PIV,” in *Particle Image Velocimetry*, 2013.
- [17] B. Wieneke, “Stereo-PIV using self-calibration on particle images,” in *Experiments in Fluids*, 2005.
- [18] J. W. Goodman, *Introduction to Fourier Optics 3ed*. 2005.



- [19] F. Scarano, L. David, M. Bsibsi, and D. Calluaud, “S-PIV comparative assessment: Image dewarping+misalignment correction and pinhole+geometric back projection,” in *Experiments in Fluids*, 2005.
- [20] A. K. Prasad and R. J. Adrian, “Stereoscopic particle image velocimetry applied to liquid flows,” *Exp. Fluids*, 1993.
- [21] G. E. Elsinga, F. Scarano, B. Wieneke, and B. W. Van Oudheusden, “Tomographic particle image velocimetry,” *Exp. Fluids*, vol. 41, no. 6, pp. 933–947, 2006.
- [22] M. Novara, K. J. Batenburg, and F. Scarano, “Motion tracking-enhanced MART for tomographic PIV,” *Meas. Sci. Technol.*, 2010.
- [23] D. P. Hart, “PIV error correction,” *Exp. Fluids*, 2000.
- [24] A. Sciacchitano and B. Wieneke, “PIV uncertainty propagation,” *Meas. Sci. Technol.*, vol. 27, no. 8, 2016.
- [25] B. Wieneke, “PIV uncertainty quantification from correlation statistics,” *Meas. Sci. Technol.*, vol. 26, no. 7, 2015.
- [26] B. W. Van Oudheusden, “PIV-based pressure measurement,” *Meas. Sci. Technol.*, 2013.
- [27] R. Gurka, A. Liberzon, and D. Hefetz, “Computation of pressure distribution using PIV velocity data,” in *Proceedings of the 3rd International Workshop on PIV*, 1999.

